Supporting Information

Facilely prepared aggregation-induced emission (AIE) nanocrystals with deep-red emission for super-resolution imaging

Ruohan Xu,[a] Dongfeng Dang,*[,a] Zhi Wang,[a] Yu Zhou,[b,c] Yanzi Xu,[a] Yizhen Zhao,[b] Xiaochi Wang,[a] Zhiwei Yang,[b] and Lingjie Meng*[,a,c]

[a] School of Chemistry, Xi'an Key Laboratory of Sustainable Energy Material Chemistry, Xi'an Jiao Tong University, Xi'an, 710049, P. R. China.

[b] School of Physics, Xi'an Jiao Tong University, Xi'an, 710049, P. R. China.

[c] Instrumental Analysis Center, Xi'an Jiao Tong University, Xi'an, 710049, P. R. China.

Corresponding author:

Prof. Dongfeng Dang and Prof. Lingjie Meng

E-mail addresses: dongfengdang@xjtu.edu.cn and menglingjie@xjtu.edu.cn

Synthetic Procedures

The synthetic procedures to DTPA-BT-H, DTPA-BT-MO, and DTPA-BT-F are depicted in Scheme S1. Their molecular structures were also characterized by ^{1}H NMR, ^{13}C NMR and HR-MS.

Synthesis of DTPA-BT-H

To a 250 mL flask, compound 1 (4-Methoxy-N-(4-methoxyphenyl)-N-(4-(4,4,5,5-tetramethyl-1,3,2-dioxaborolan-2-yl)phenyl)aniline, 2.5 mmol, 1.08 g), compound 2 (4,7-dibromo-2,1,3-benzothiadiazole, 1 mmol, 294 mg), ethanol (10 mL), $Pd(PPh_3)_4$ (Tetrakis-(triphenylphosphine)palladium, 0.05 mmol, 57 mg) and K_2CO_3 (2 M, 12.5 mL) were added into toluene solution (70 mL) under a N_2 atmosphere. Then, the reaction mixture was stirred at 80 °C for 20 h. After cooling down, the mixture was extracted with dichloromethane (DCM) for three times (3×70 mL), and the obtained organic phase was washed with water (3×70 mL). Then, the solvent was removed under vacuum and the crude compound was purified by column chromatography (DCM/petroleum ether= 2/1, *v*/*v*) to get a pure DTPA-BT-H (535 mg, 72%). ^{1}H NMR (600 MHz, Chloroform-*d*) δ 7.82 (d, J = 8.82 Hz, 4H), 7.69 (s, 2H), 7.15 (d, J = 8.94 Hz, 8H), 7.06 (d, J = 8.76 Hz, 4H), 6.87 (d, J = 8.94 Hz, 8H), 3.81 (s, 12H). ^{13}C NMR (150 MHz, Chloroform-*d*) δ 156.09, 154.21, 148.78, 140.58, 132.02, 129.67, 129.09, 126.98, 119.80, 114.73, 55.49 ppm. HR-MS (TOF-ESI+): *m*/*z* calculated for $[M]^+$ $C_{46}H_{38}N_4O_4S$, 742.26138; Found, 742.26117. *m*/*z* calculated for $[M]^{2+}$ $C_{46}H_{38}N_4O_4S$, 371.13069; Found, 371.12916.

Synthesis of DTPA-BT-MO

The synthetic procedure to DTPA-BT-MO is similar to that in DTPA-BT-H. The only difference is that compound 2 is changed to be compound 3 (4,7-dibromo-5,6-methoxy-2,1,3-benzothiadiazole). The yield is 68% here (546

mg). ^{1}H NMR (600 MHz, Chloroform-*d*) δ 7.55 (d, J = 8.76 Hz, 4H), 7.17 (d, J = 8.88 Hz, 8H), 7.04 (d, J = 8.76 Hz, 4H), 6.87 (d, J = 8.94 Hz, 8H), 3.81 (s, 18H). ^{13}C NMR (150 MHz, Chloroform-*d*) δ 156.11, 153.27, 152.35, 148.41, 140.59, 131.05, 127.20, 124.73, 123.58, 118.89, 114.72, 61.34, 55.48 ppm. HR-MS (TOF-ESI+): *m*/*z* calculated for $[M+H]^+$ $C_{48}H_{42}N_4O_6S$, 803.29033; Found, 803.28715.

Synthesis of DTPA-BT-F

The synthetic procedure to DTPA-BT-F is similar to that in DTPA-BT-H. The only difference is that compound 2 is changed to be compound 4 (4,7-dibromo-5,6-fluorine-2,1,3-benzothiadiazole). The yield is 75% here (584 mg). ^{1}H NMR (600 MHz, Chloroform-*d*) δ 7.67 (d, J = 8.76 Hz, 4H), 7.17 (d, J = 8.94 Hz, 8H), 7.04 (d, J = 8.88 Hz, 4H), 6.88 (d, J = 8.94 Hz, 8H), 3.81 (s, 12H). ^{13}C NMR (150 MHz, Chloroform-*d*) δ 156.41, 149.29, 140.22, 131.18, 127.42, 121.31, 118.68, 114.83, 55.51 ppm. HR-MS (TOF-ESI+): *m*/*z* calculated for $[M+H]^+$ $C_{46}H_{36}F_2N_4O_4S$, 779.25036; Found, 779.24673.

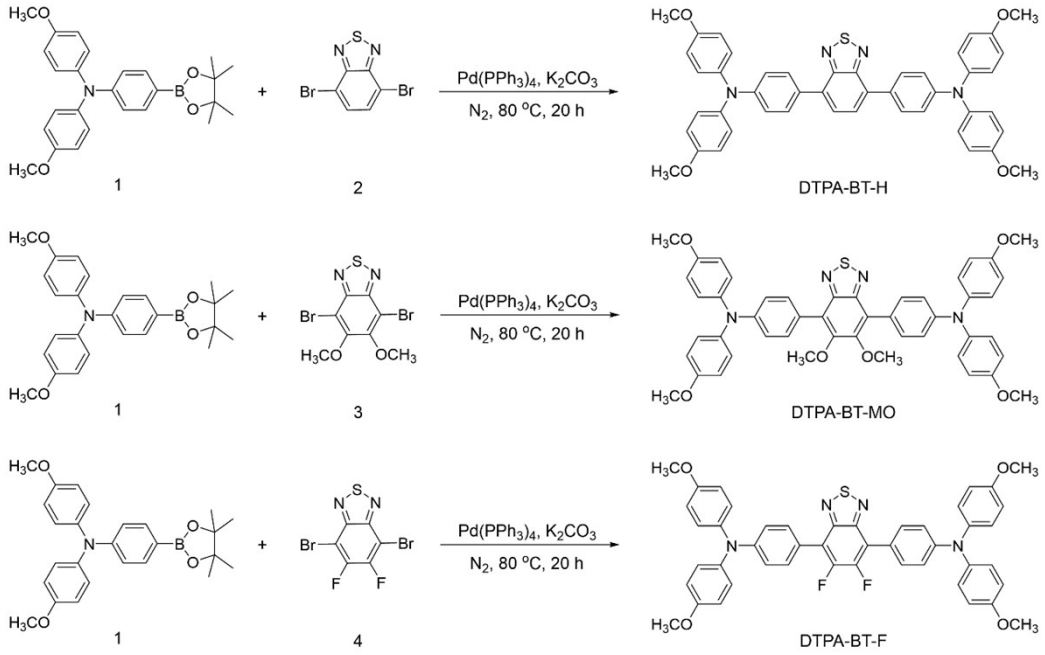

Scheme S1. The synthetic route to DTPA-BT-H, DTPA-BT-MO, and DTPA-BT-F.

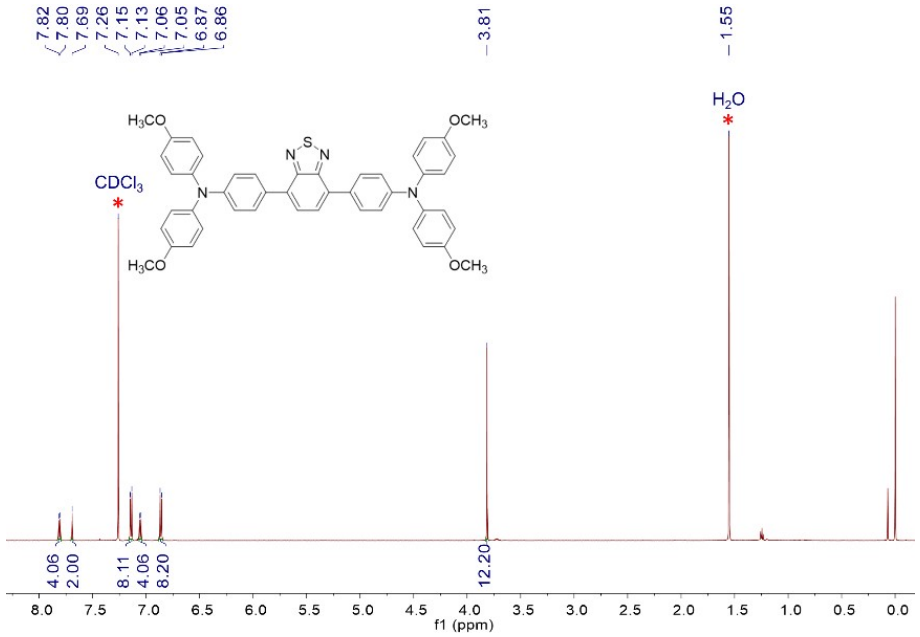

Figure S1. ^{1}H NMR spectrum of DTPA-BT-H.

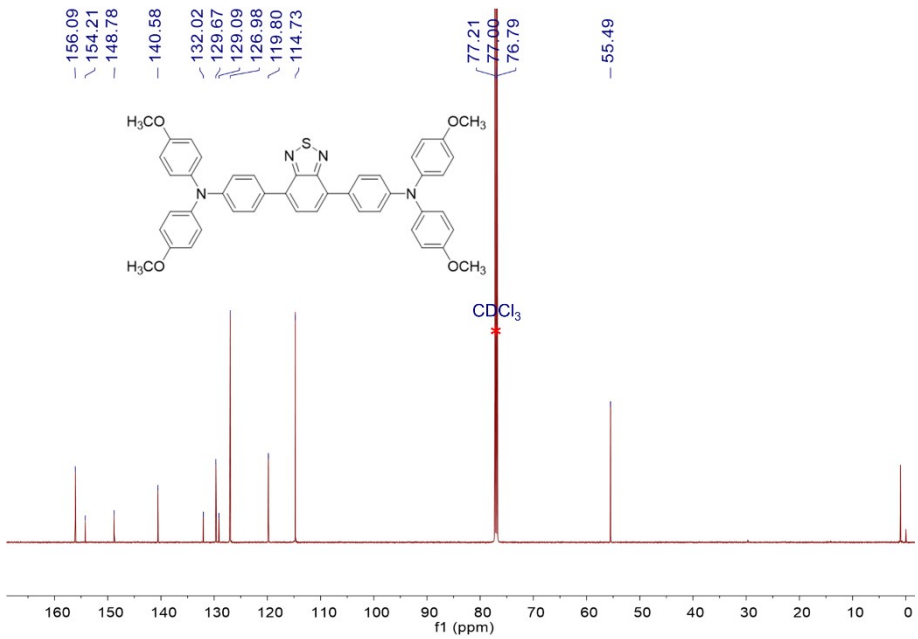

Figure S2. ^{13}C NMR spectrum of DTPA-BT-H.

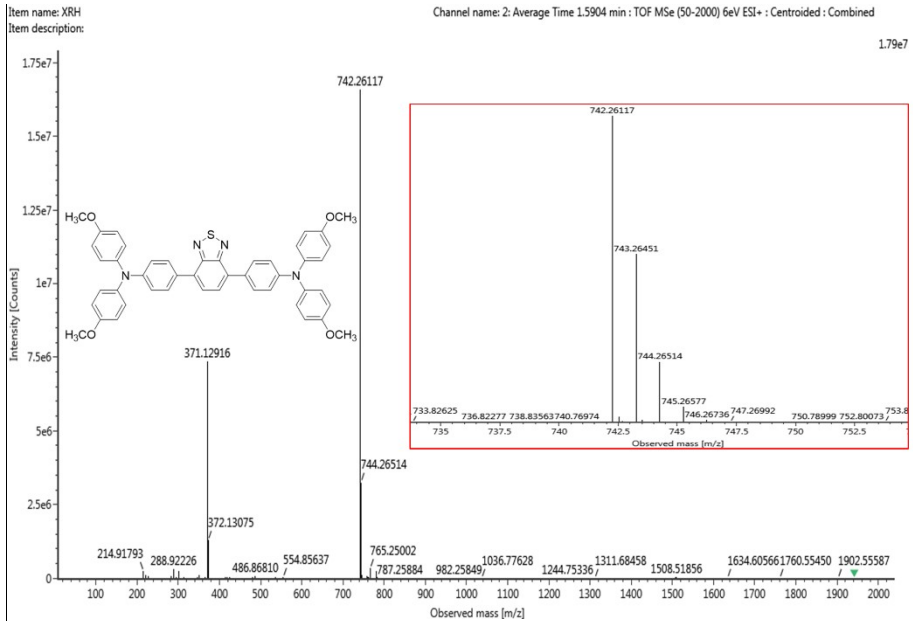

Figure S3. HR-MS spectrum of DTPA-BT-H.

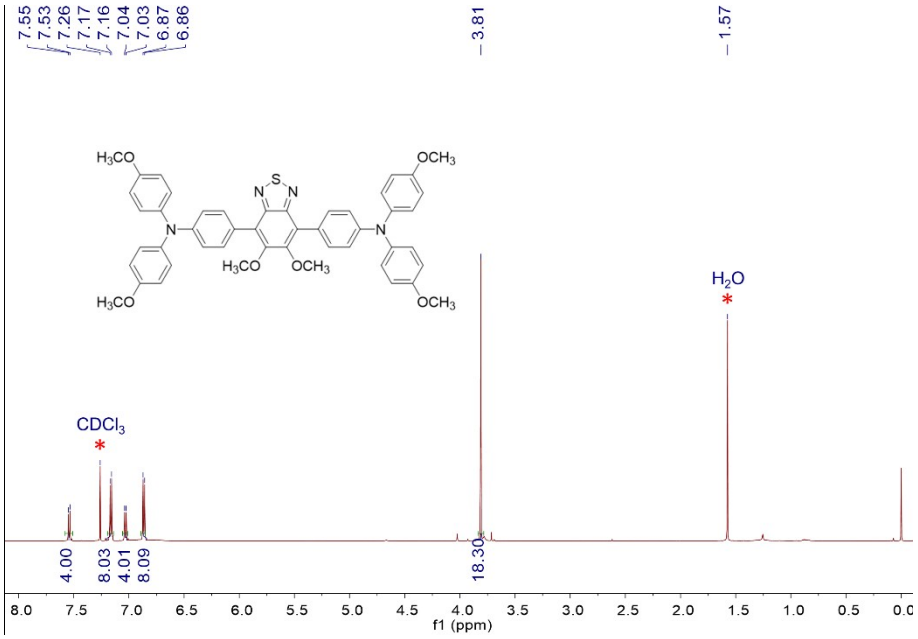

Figure S4. ^{1}H NMR spectrum of DTPA-BT-MO.

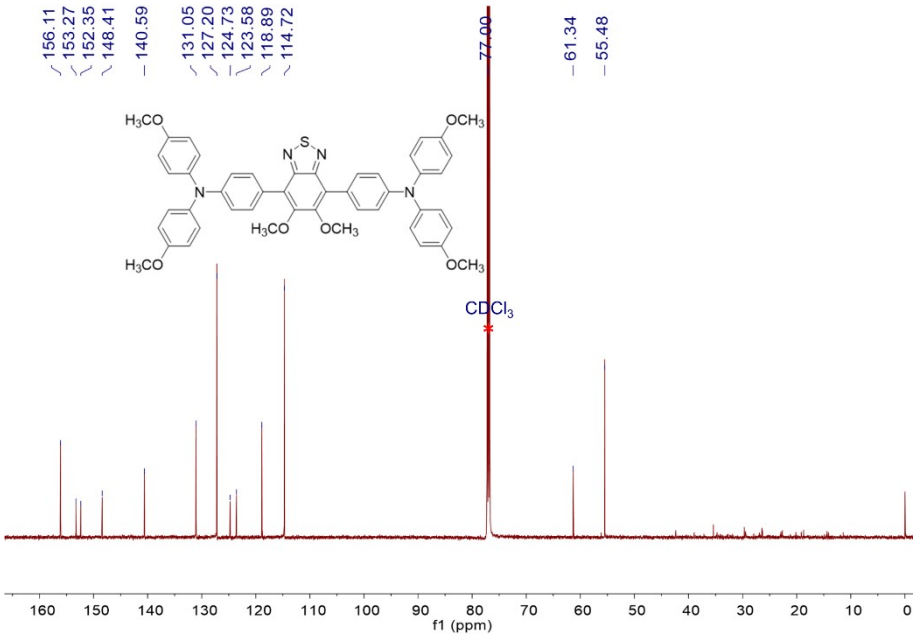

Figure S5. ^{13}C NMR spectrum of DTPA-BT-MO.

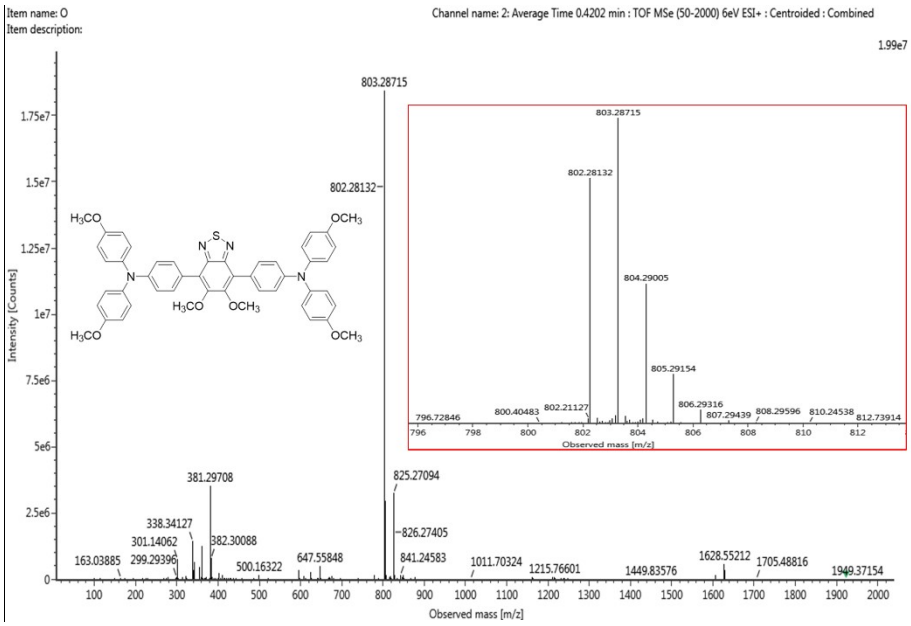

Figure S6. HR-MS spectrum of DTPA-BT-MO.

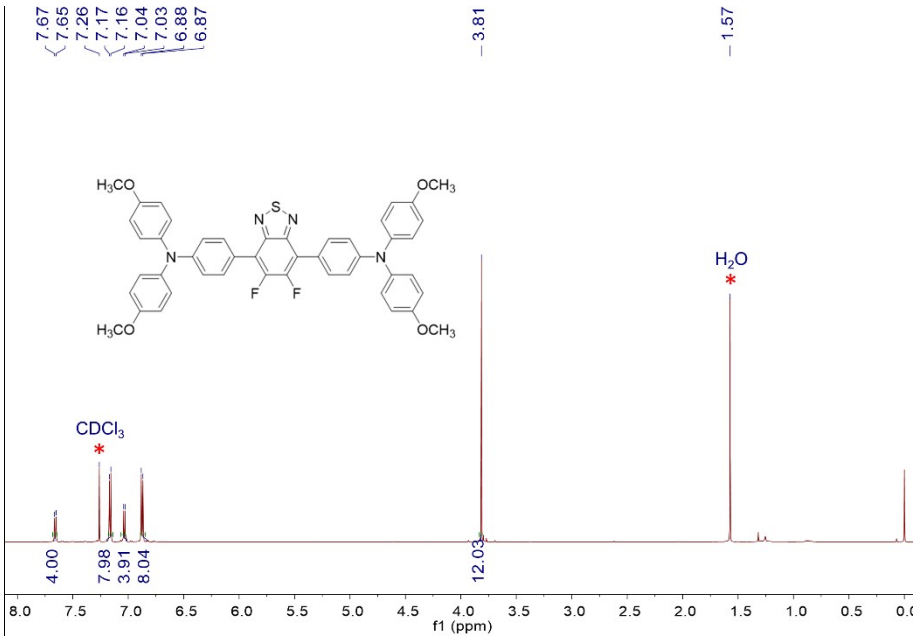

Figure S7. ^{1}H NMR spectrum of DTPA-BT-F.

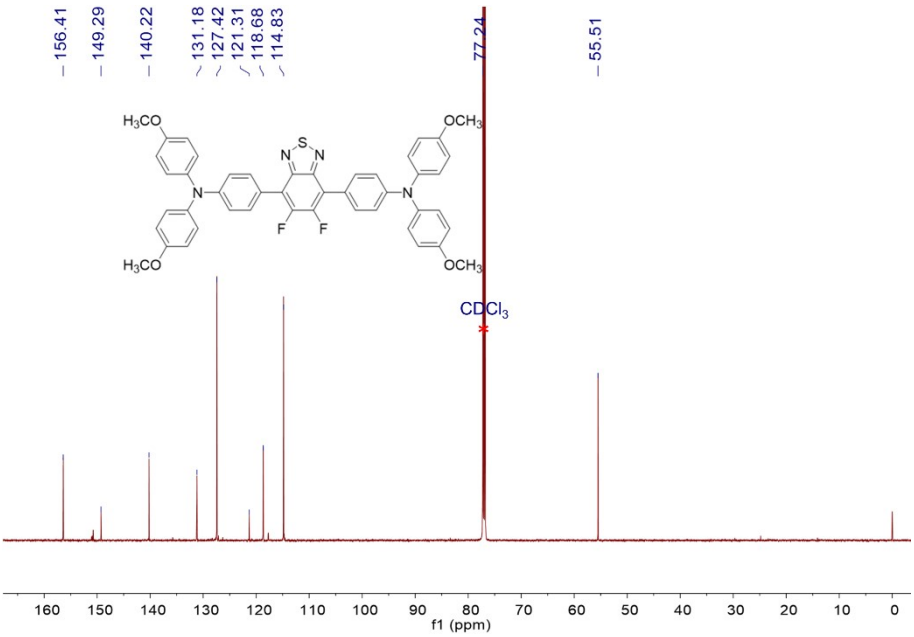

Figure S8. ^{13}C NMR spectrum of DTPA-BT-F.

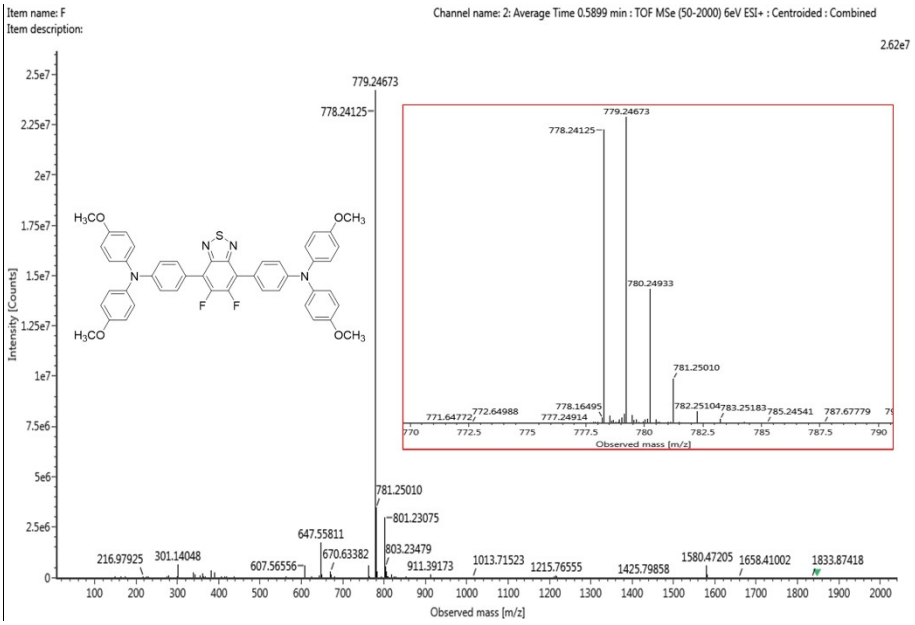

Figure S9. HR-MS spectrum of DTPA-BT-F.

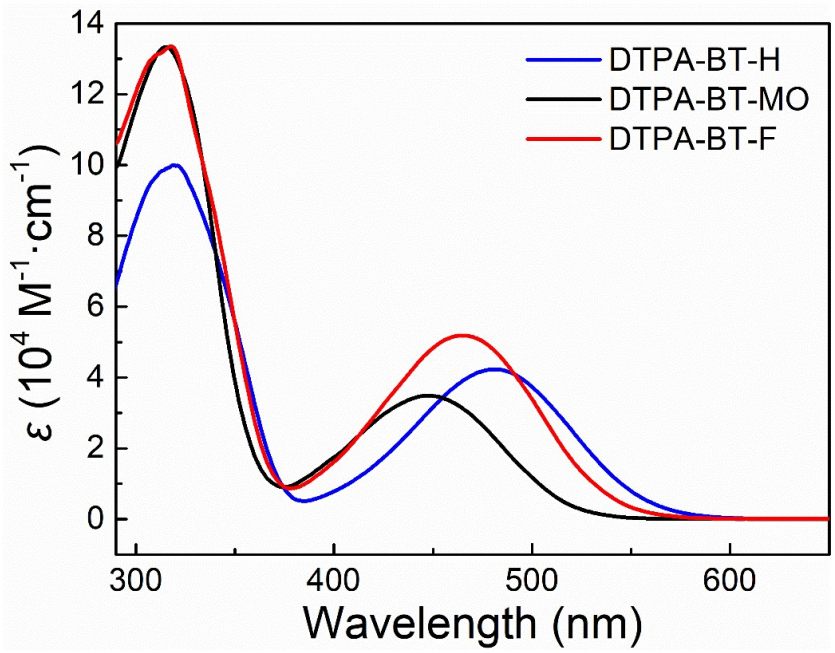

Figure S10. UV-vis spectra of DTPA-BT-H, DTPA-BT-MO and DTPA-BT-F in THF ([*c*]= 1×10^{-5} M).

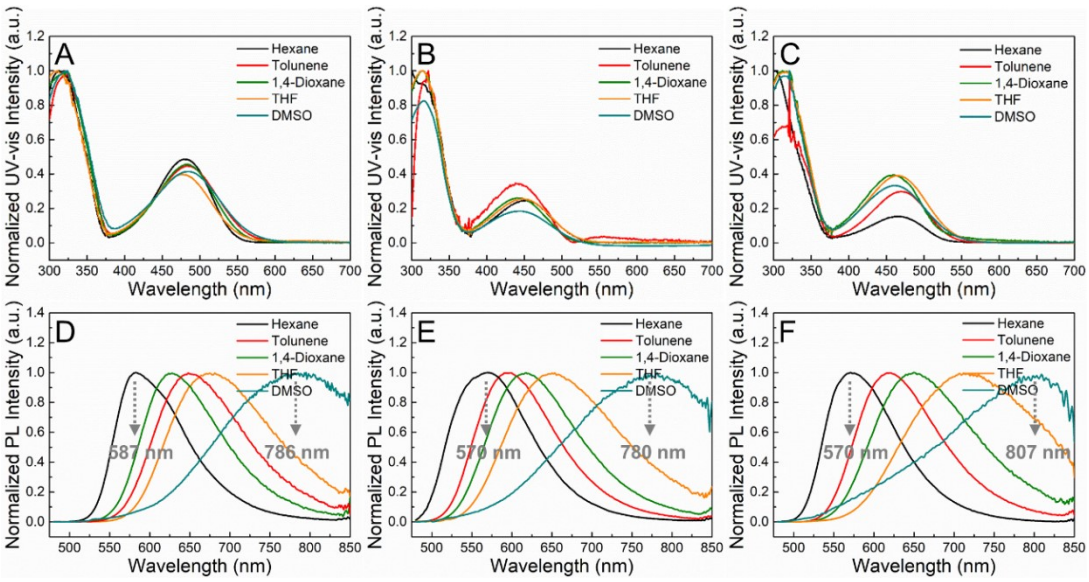

Figure S11. Normalized UV-vis spectra (A-C) and normalized PL spectra (D-F) of DTPA-BT-H (A and D), DTPA-BT-MO (B and E) and DTPA-BT-F (C and F) in solvents with varied polarities.

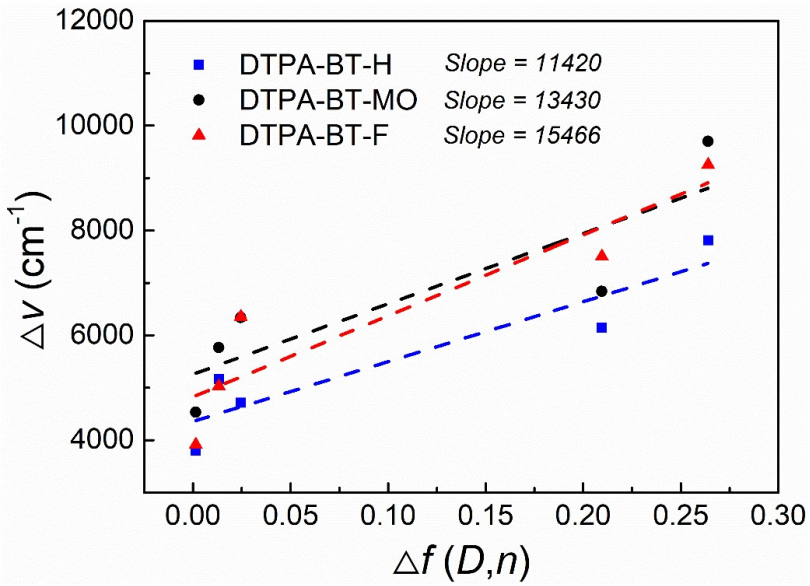

Figure S12. Plot of Stokes' shift (Δv) *vs*. Δf for DTPA-BT-H, DTPA-BT-MO and DTPA-BT-F in solvents with varied polarities.

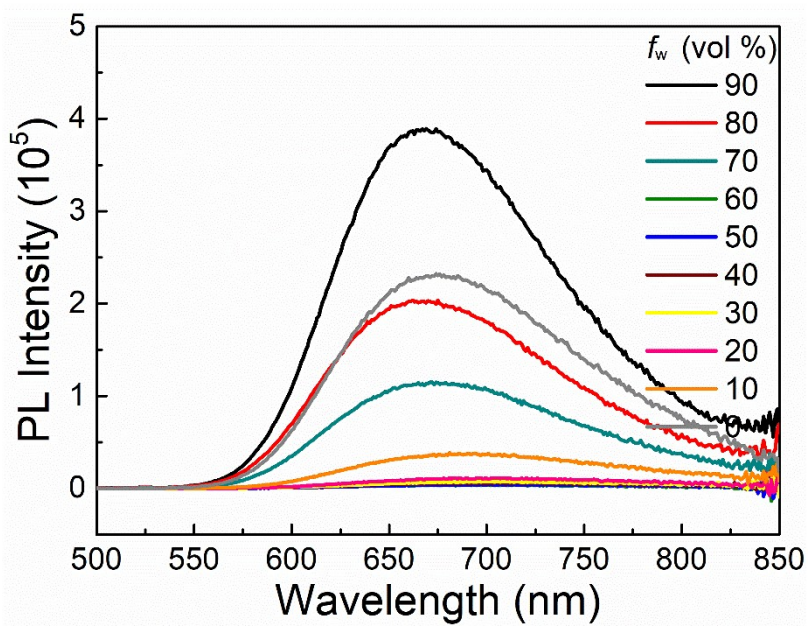

Figure S13. PL spectra of DTPA-BT-H in THF/water mixtures with different f_w ([c]= 1×10^{-5} M).

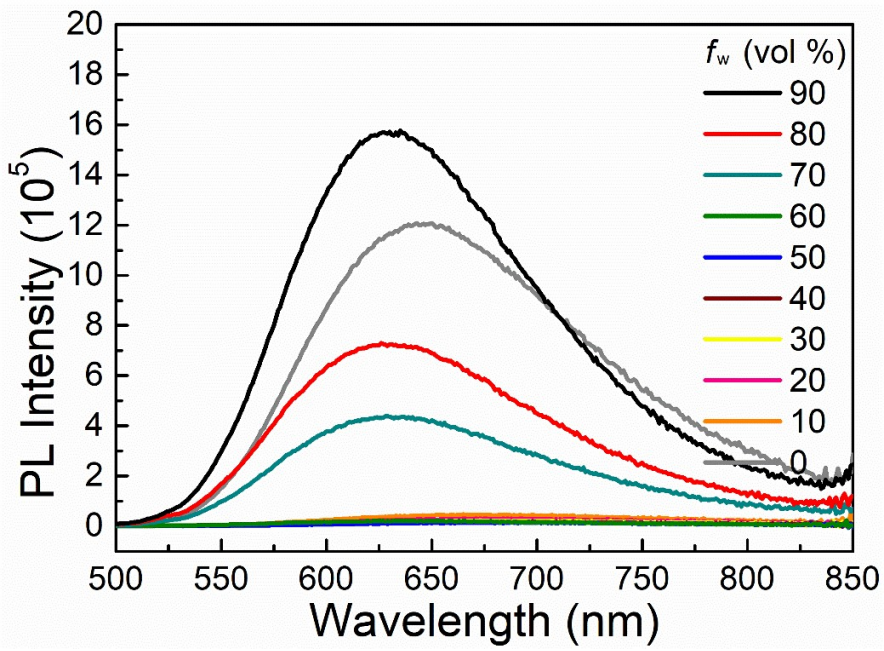

Figure S14. PL spectra of DTPA-BT-MO in THF/water mixtures with different f_w ([c]= 1×10^{-5} M).

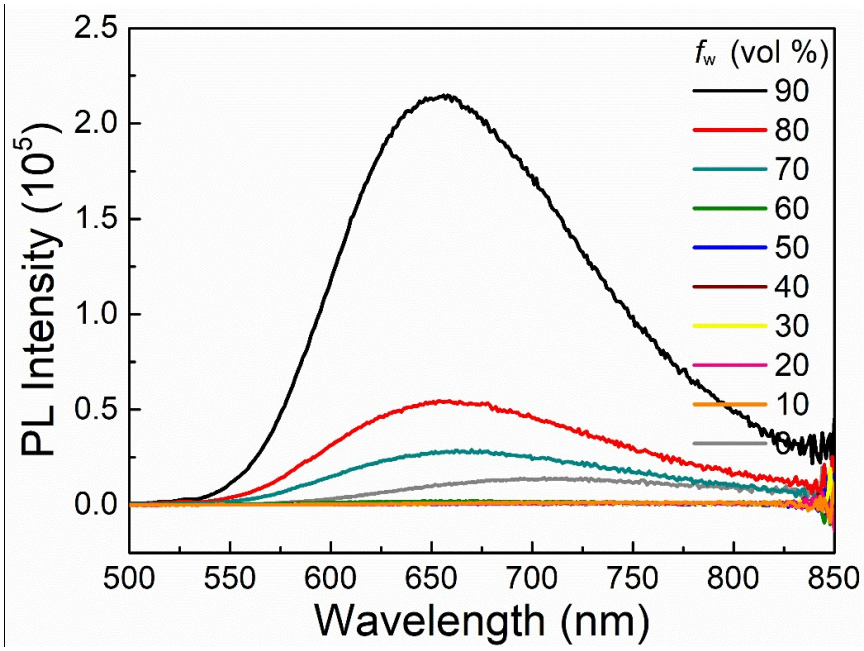

Figure S15. PL spectra of DTPA-BT-F in THF/water mixtures with different f_w ([c]= 1×10^{-5} M).

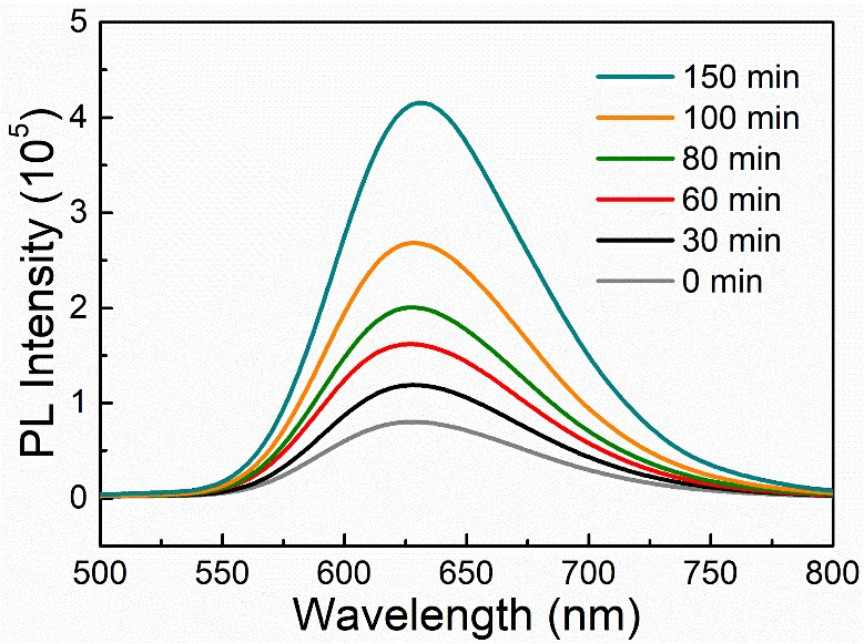

Figure S16. Time-dependent fluorescence spectra of DTPA-BT-H in THF/water mixture ([*c*]= 2×10^{-5} M, f_w= 60%).

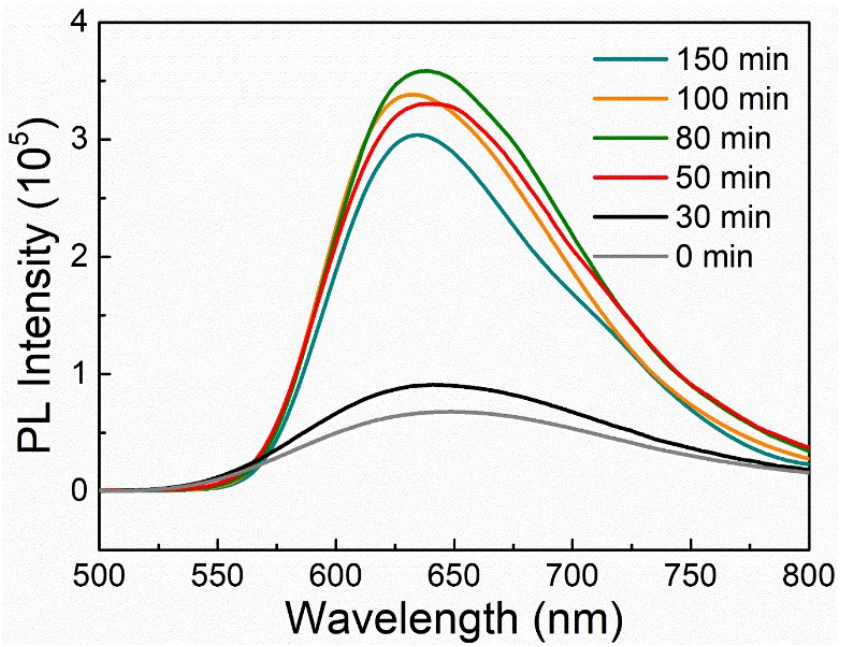

Figure S17. Time-dependent fluorescence spectra of DTPA-BT-MO in THF/water mixture ([*c*]= 2×10^{-5} M, f_w= 60%).

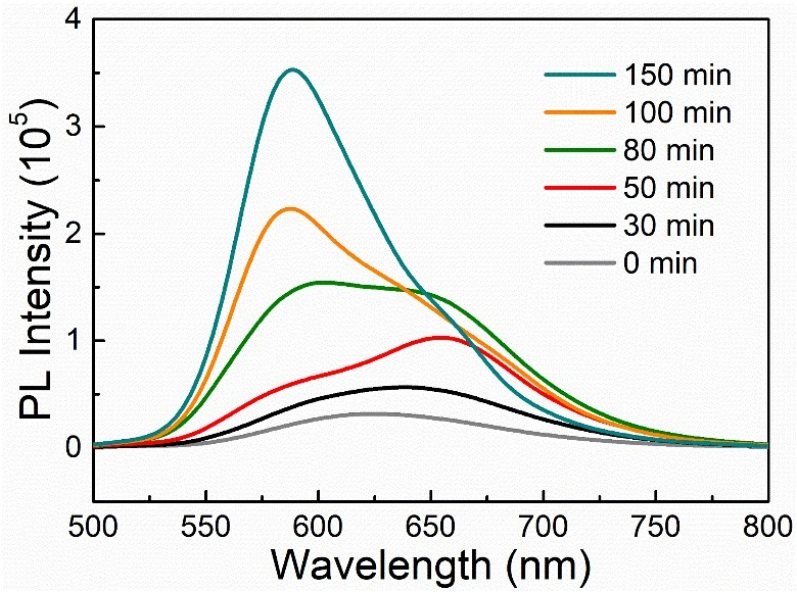

Figure S18. Time-dependent fluorescence spectra of DTPA-BT-F in THF/water mixture ([*c*]= 2×10^{-5} M, f_w= 60%).

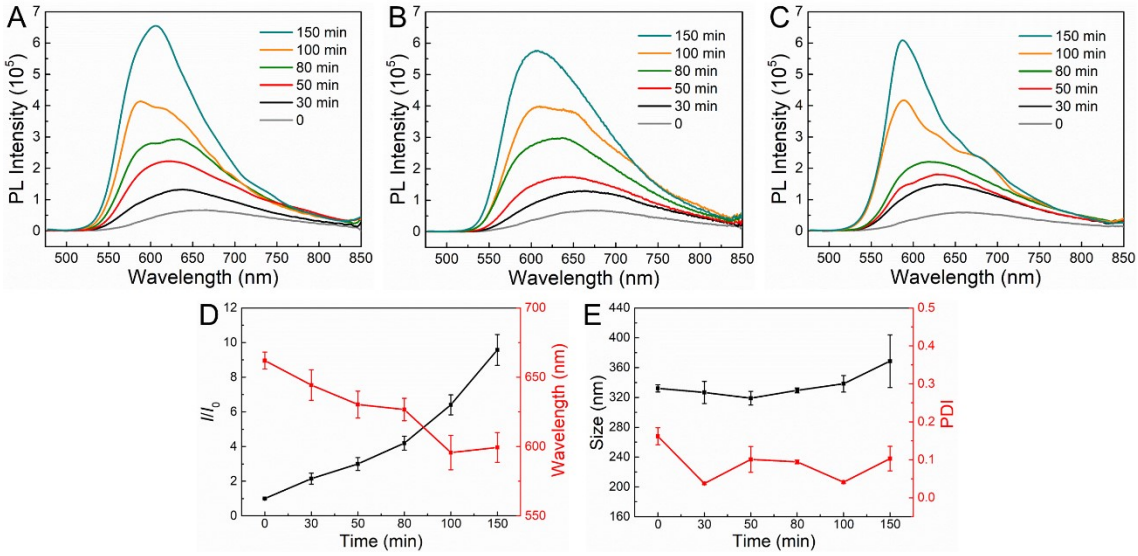

Figure S19. Time-dependent PL spectra of DTPA-BT-F in THF/water mixture (three parallel experiments; [*c*]= 2×10^{-5} M, f_w= 60%; A-C); Plots of I/I_0 values and maximum emission wavelengths for DTPA-BT-F in THF/water mixture at different time (D); Colloidal size and the corresponding PDI values for DTPA-BT-F in THF/water mixture at different time (E).

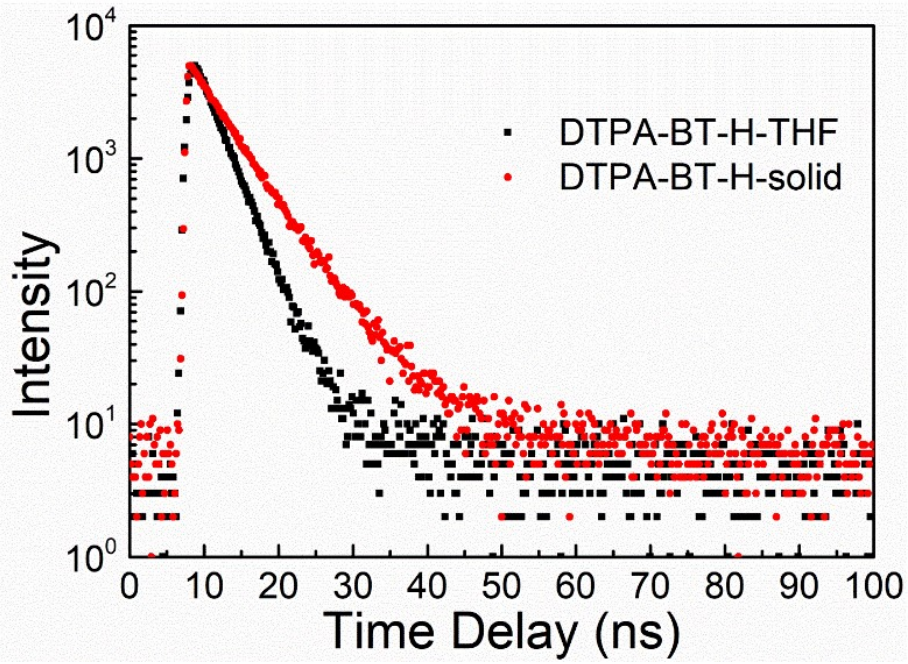

Figure S20. Transient decay spectra of DTPA-BT-H in THF solution and in solids.

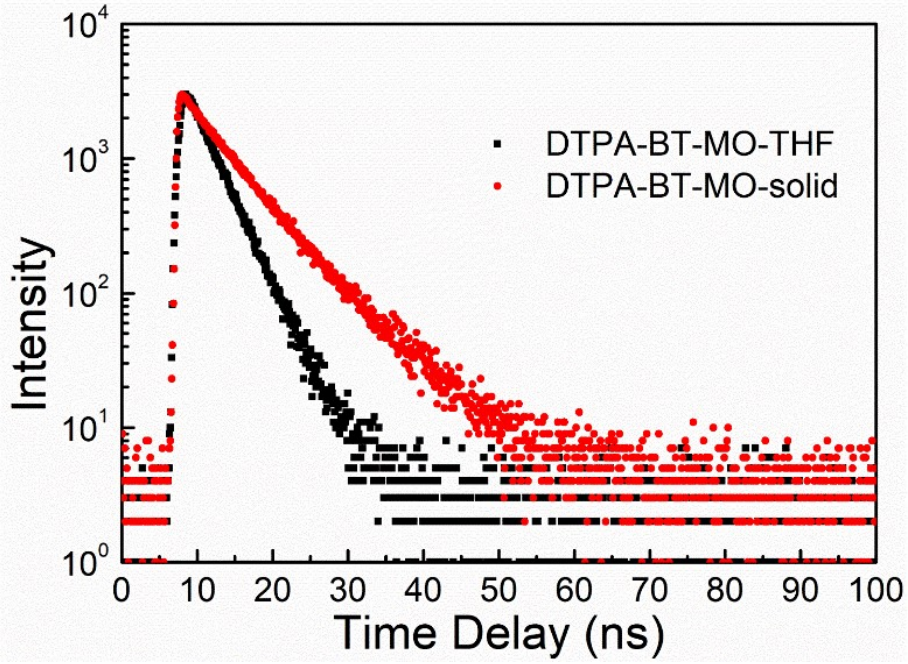

Figure S21. Transient decay spectra of DTPA-BT-MO in THF solution and in solids.

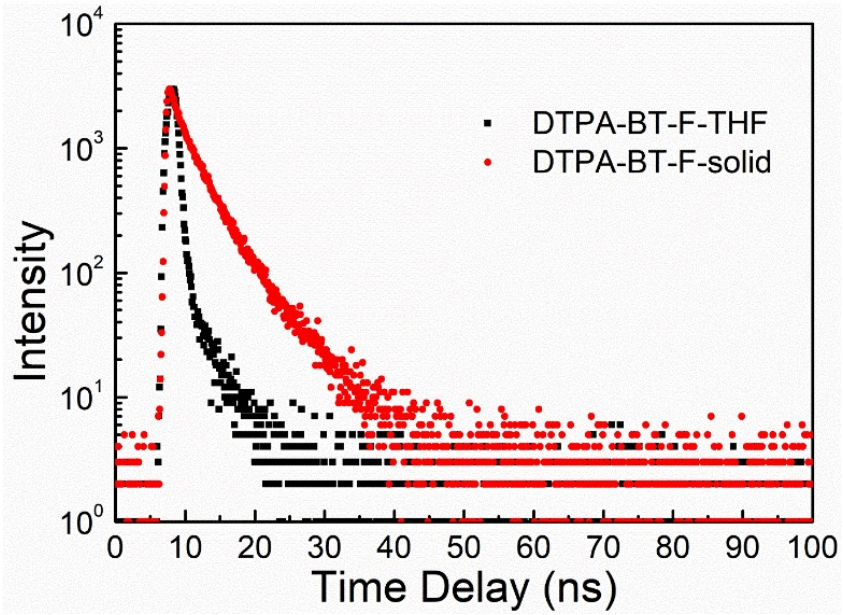

Figure S22. Transient decay spectra of DTPA-BT-F in THF solution and in solids.

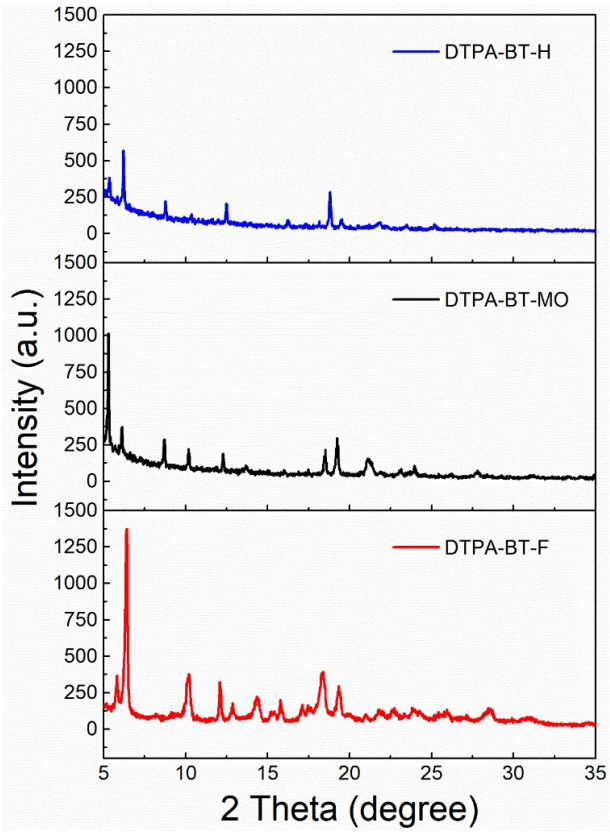

Figure S23. XRD patterns of DTPA-BT-H, DTPA-BT-MO and DTPA-BT-F in pristine powder.

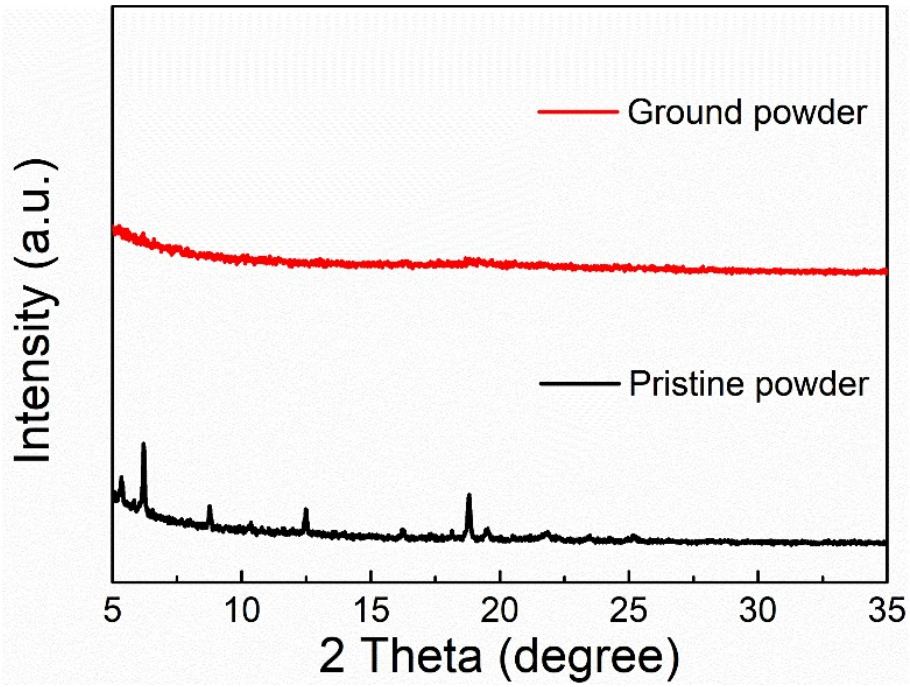

Figure S24. XRD patterns of DTPA-BT-H powder before and after grinding.

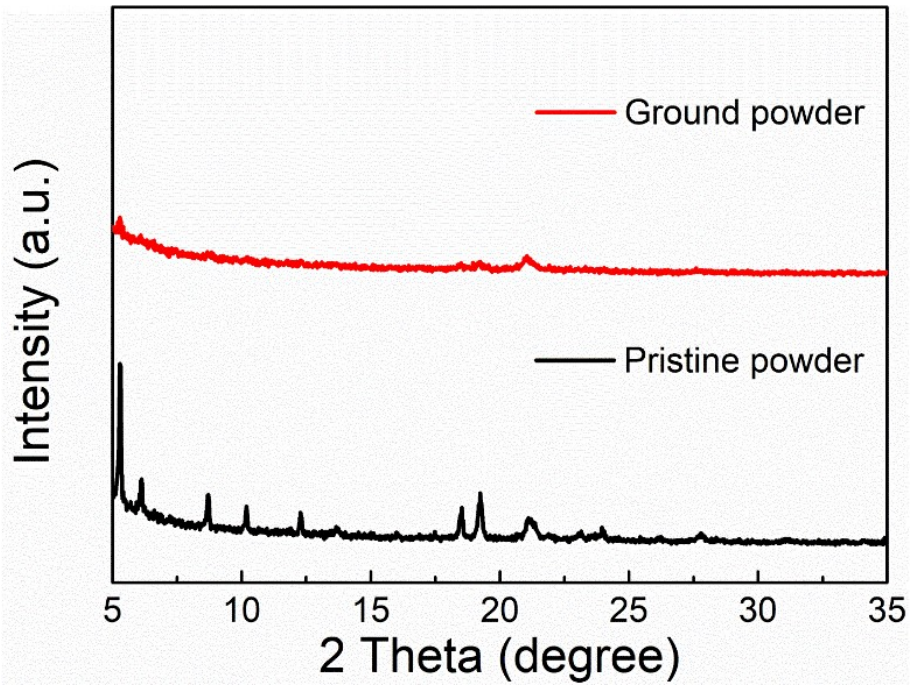

Figure S25. XRD patterns of DTPA-BT-MO powder before and after grinding.

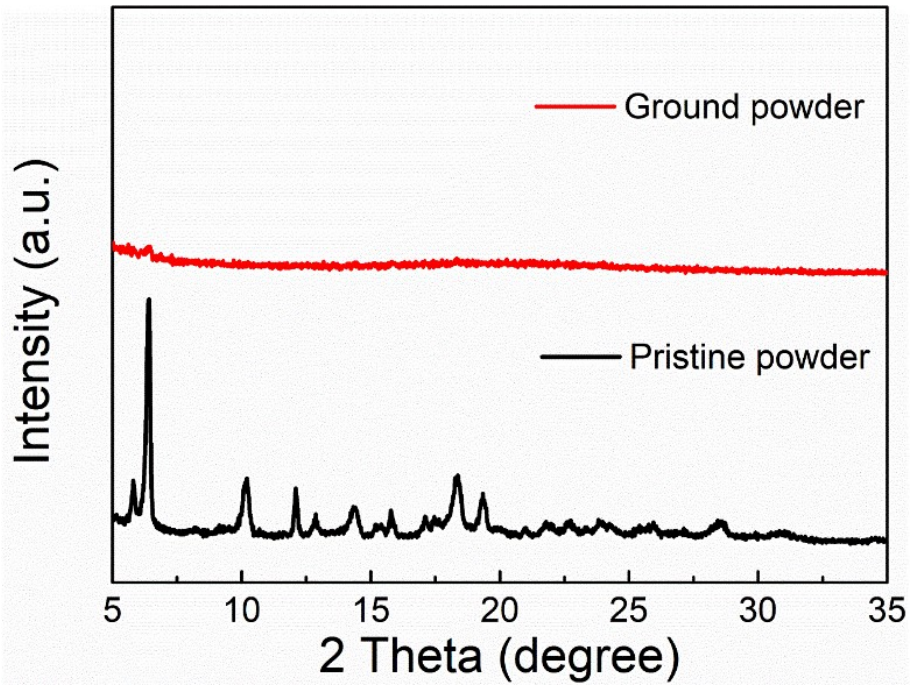

Figure S26. XRD patterns of DTPA-BT-F powder before and after grinding.

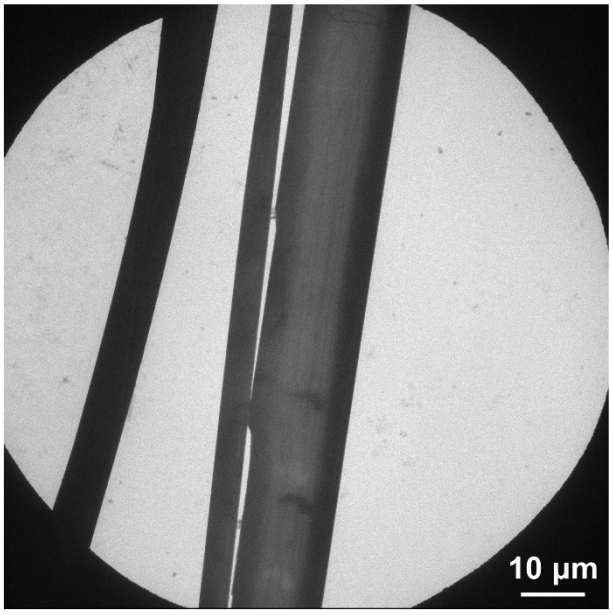

Figure S27. TEM image of large sized precipitations by DTPA-BT-F in THF/water mixture (f_w= 60%) when stored for 6 d.

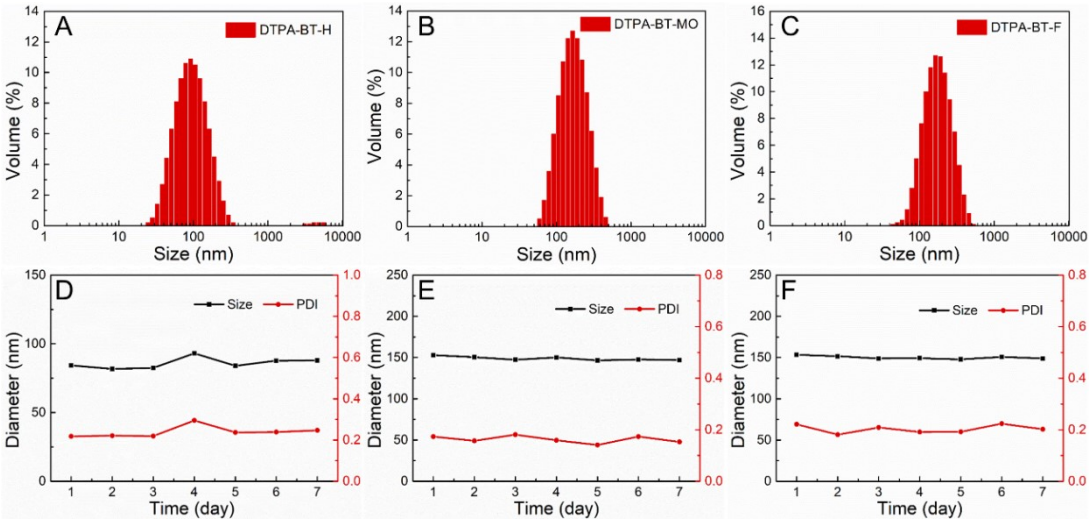

Figure S28. Particle size distribution of DTPA-BT-H NPs (A), DTPA-BT-MO NPs (B) and DTPA-BT-F NCs (C); Their corresponding colloidal stability of size and PDI values over 7 d (D-F).

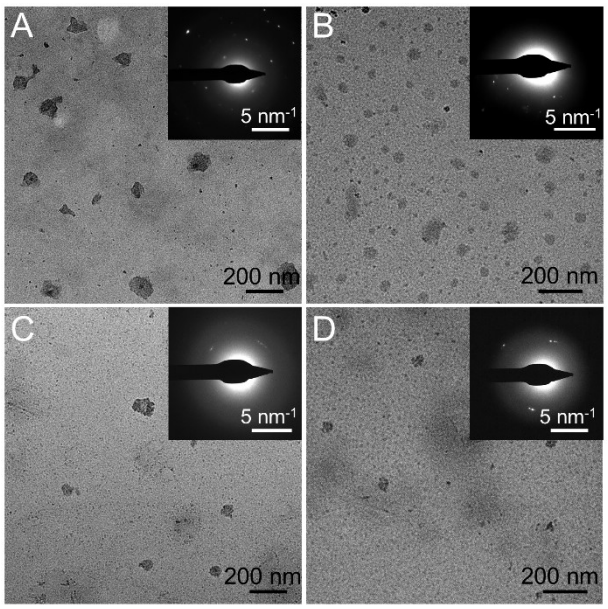

Figure S29. TEM image of freshly-prepared DTPA-BT-F NCs (A and C) and room temperature-stored DTPA-BT-F NCs (B and D) in water (A and B) and cell growth media (C and D).

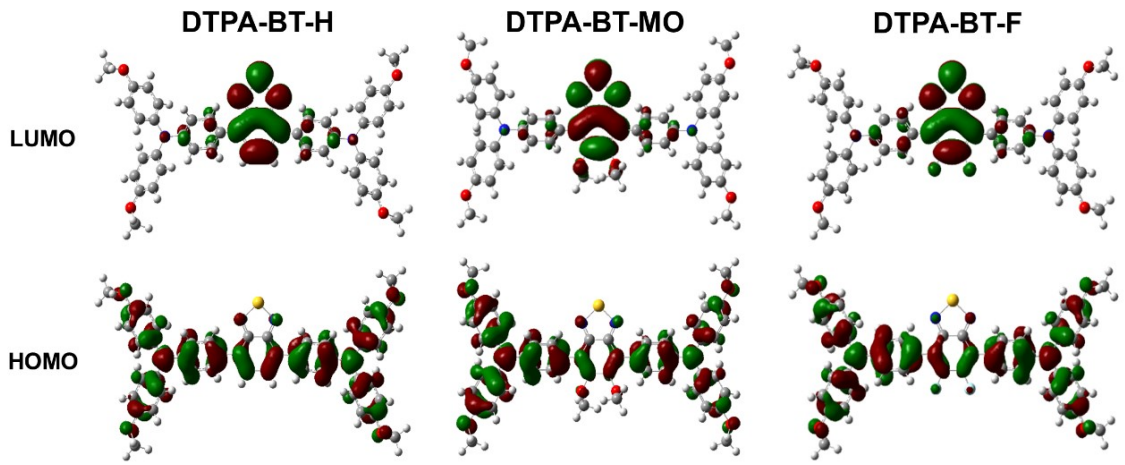

Figure S30. HOMO and LUMO energy levels of DTPA-BT-H, DTPA-BT-MO and DTPA-BT-F calculated by DFT at B3LYP/6-31G(d) level.

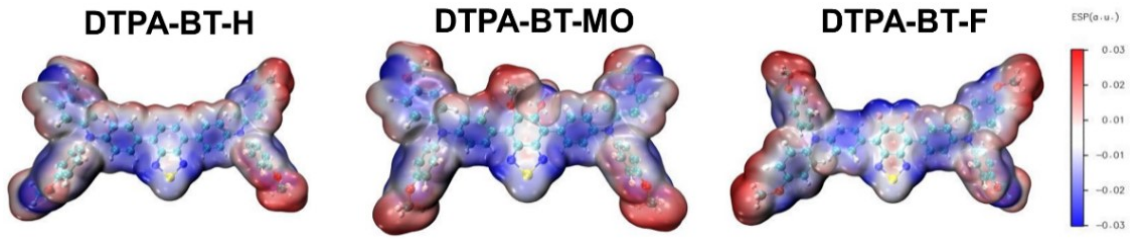

Figure S31. ESP of DTPA-BT-H, DTPA-BT-MO and DTPA-BT-F calculated by DFT at B3LYP/6-31G(d) level.

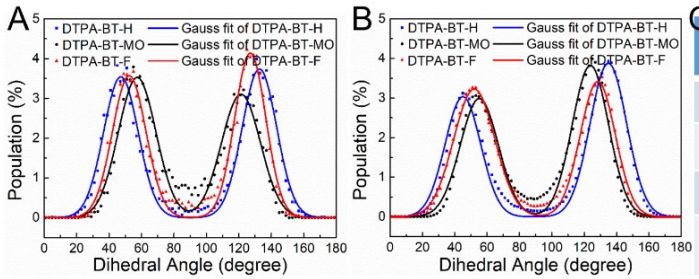

C

Sample	FWHM[a] (°)	FWHM[b] (°)
DTPA-BT-H	25.14/25.07	25.90/26.74
DTPA-BT-MO	27.63/28.48	27.80/26.59
DTPA-BT-F	24.41/22.64	30.13/25.63

[a] Calculated by MD in the single molecular state;
[b] Calculated by MD in the clustered state.

Figure S32. Dihedral angle distribution between phenyl rings a and b for DTPA-BT-H, DTPA-BT-MO and DTPA-BT-F in single molecular state (A) and aggregated state (B); The corresponding calculated FWHM values of dihedral angle distribution (C).

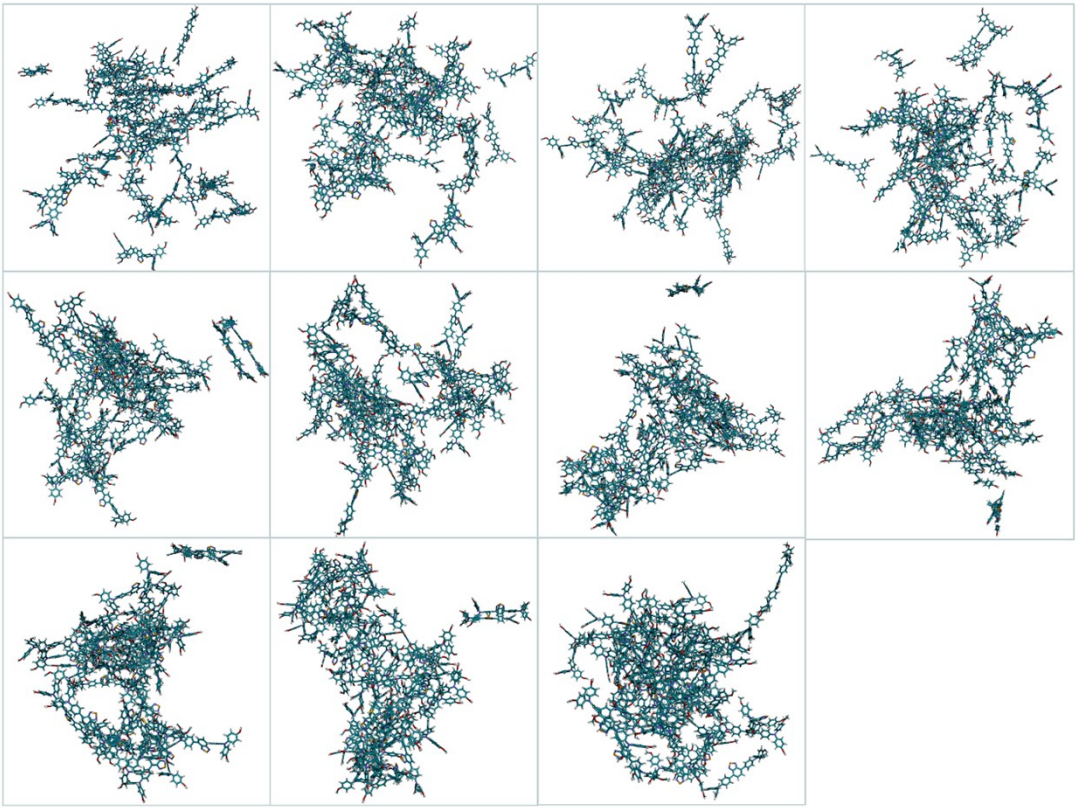

Figure S33. The cluster analysis of DTPA-BT-H simulated by AMBER18 package.

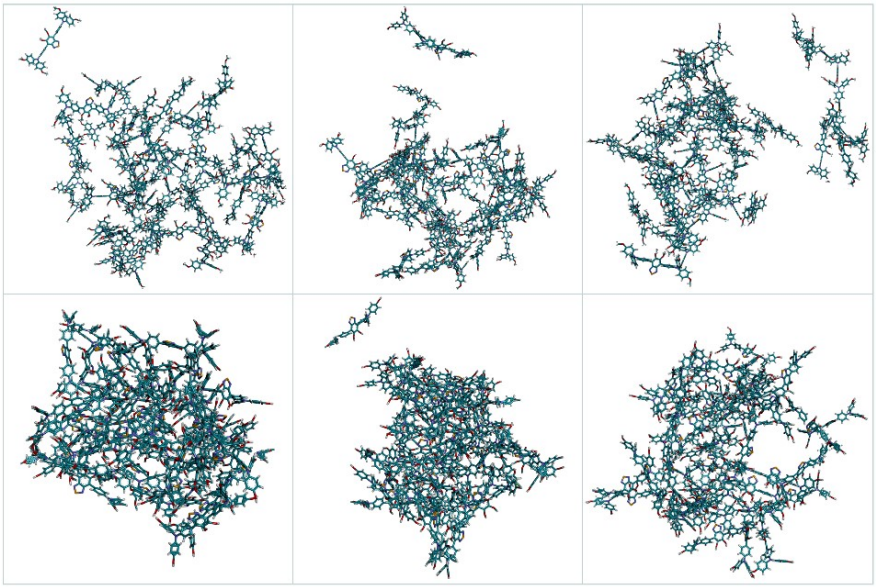

Figure S34. The cluster analysis of DTPA-BT-MO simulated by AMBER18 package.

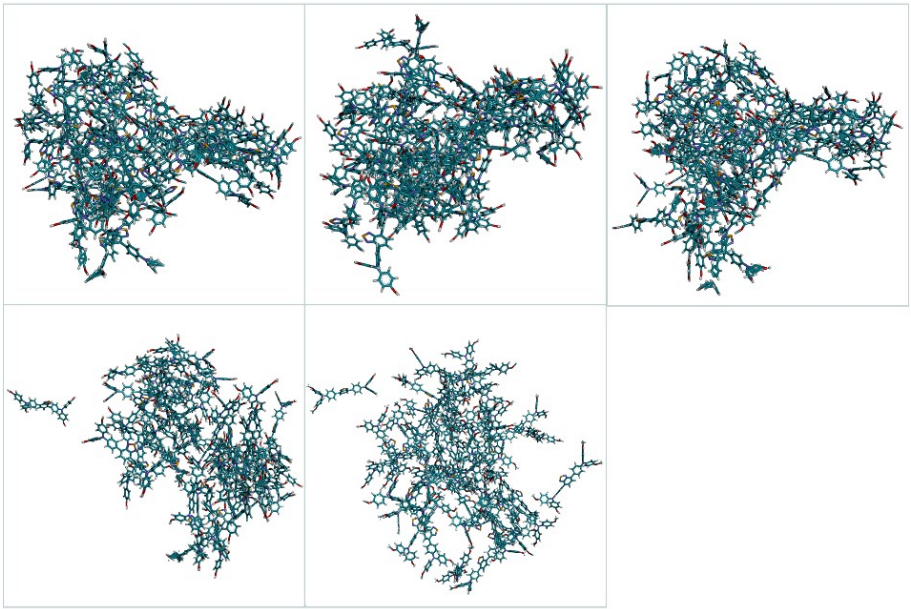

Figure S35. The cluster analysis of DTPA-BT-F simulated by AMBER18 package.

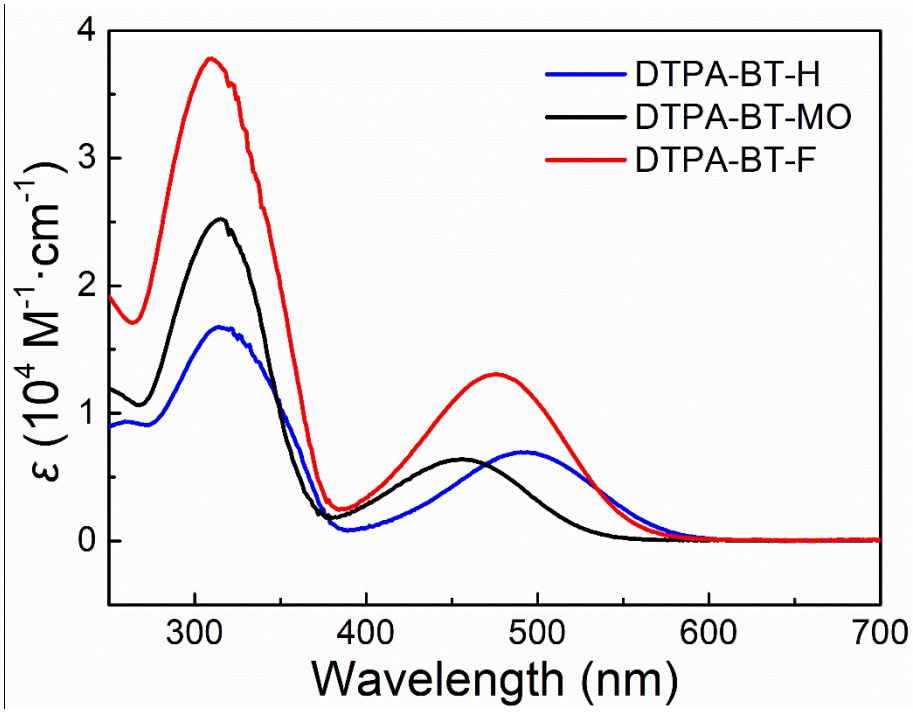

Figure S36. UV-vis spectra of DTPA-BT-H NPs, DTPA-BT-MO NPs and DTPA-BT-F NCs ([*c*]= 20 μg·mL^{-1}).

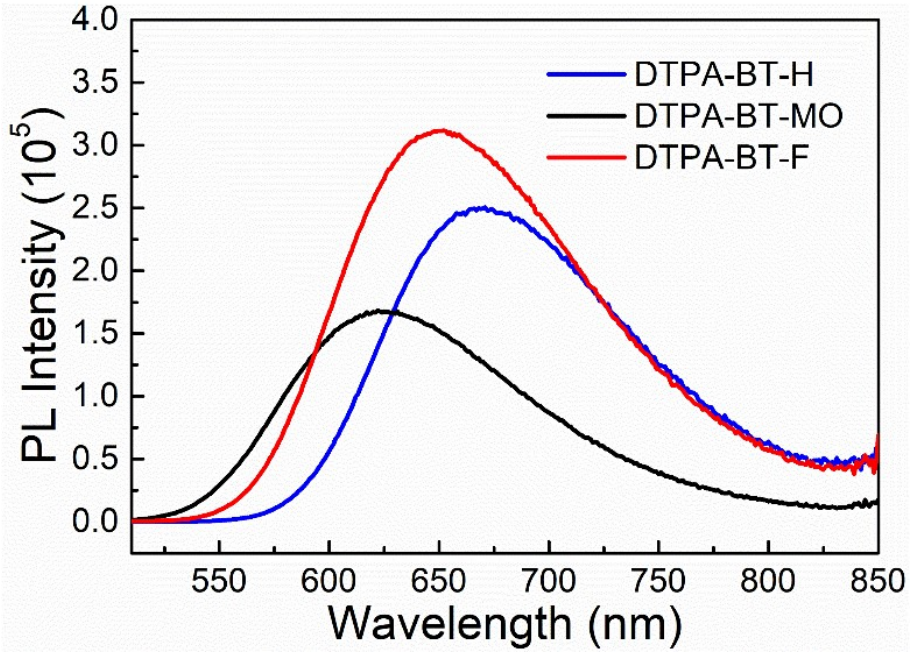

Figure S37. PL spectra of DTPA-BT-H NPs, DTPA-BT-MO NPs and DTPA-BT-F NCs ([*c*]= 20 μg·mL^{-1}).

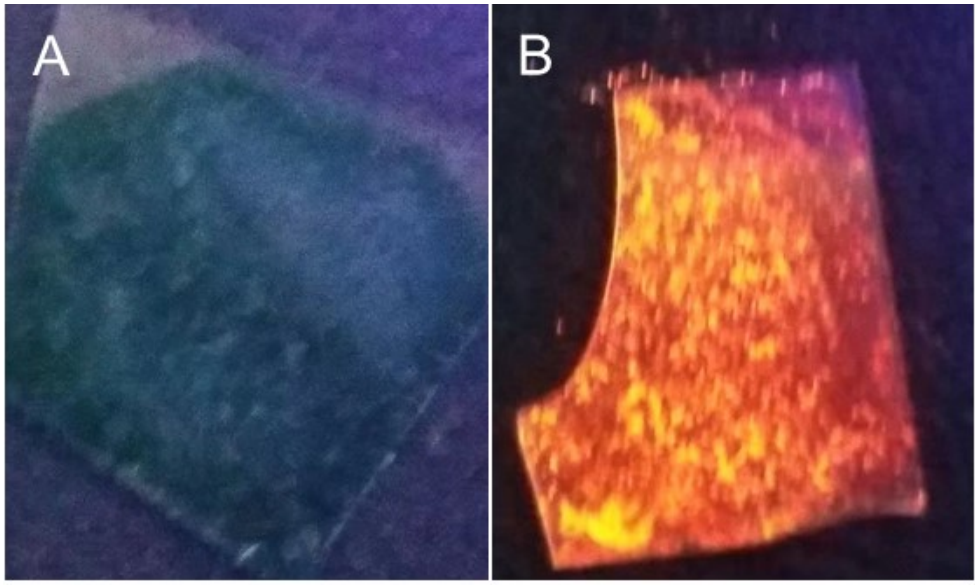

Figure S38. Fluorescence images of SiR (A) and DTPA-BT-F (B) thin film by UV lamp.

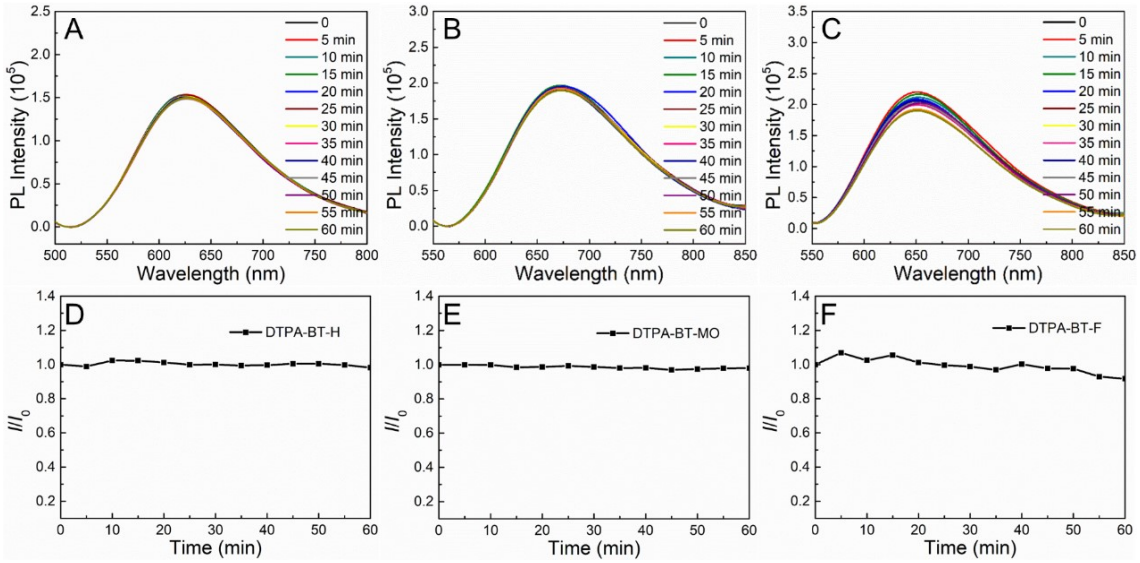

Figure S39. Time-dependent PL spectra for DTPA-BT-H NPs (A), DTPA-BT-MO NPs (B) and DTPA-BT-F NCs (C) under Xenon lamp irradiation over 1 h; Plots of I/I_0 values for DTPA-BT-H NPs (D), DTPA-BT-MO NPs (E) and DTPA-BT-F NCs (F) under Xenon lamp irradiation over 1 h.

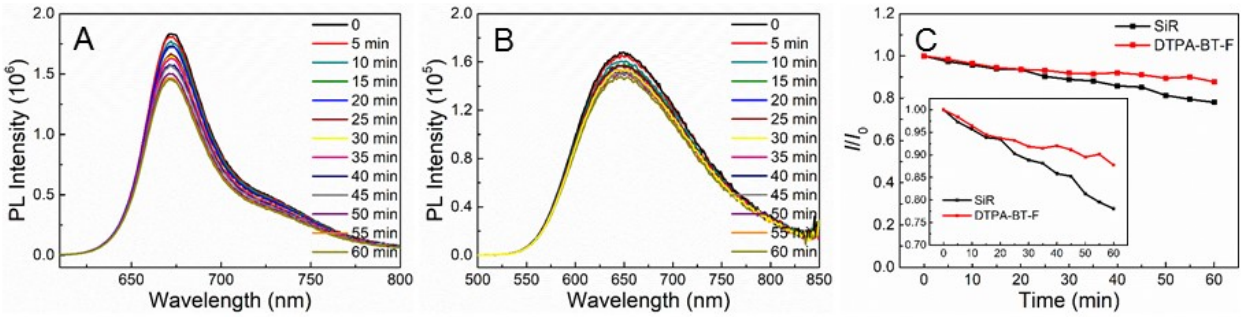

Figure S40. Time-dependent PL spectra for SiR (A), DTPA-BT-F NCs (B) and their Plots of I/I_0 values (C, the inset is an enlarged view) under high power white laser (200 mW).

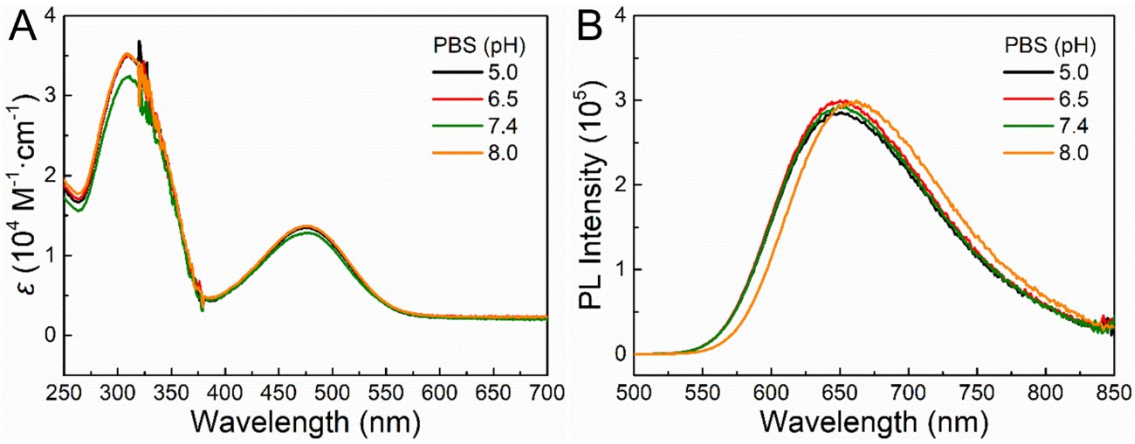

Figure S41. UV-vis spectra (A) and PL spectra (B) of DTPA-BT-F NCs dispersed in PBS solutions with different pH values ([*c*]= 20 μg·mL^{-1}).

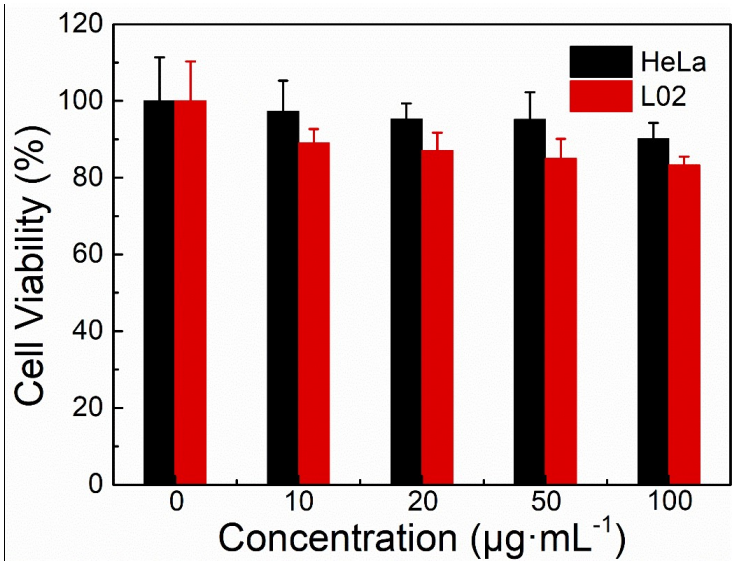

Figure S42. The viability of HeLa and L02 cells after incubation with DTPA-BT-F NCs for 24 h under different concentration.

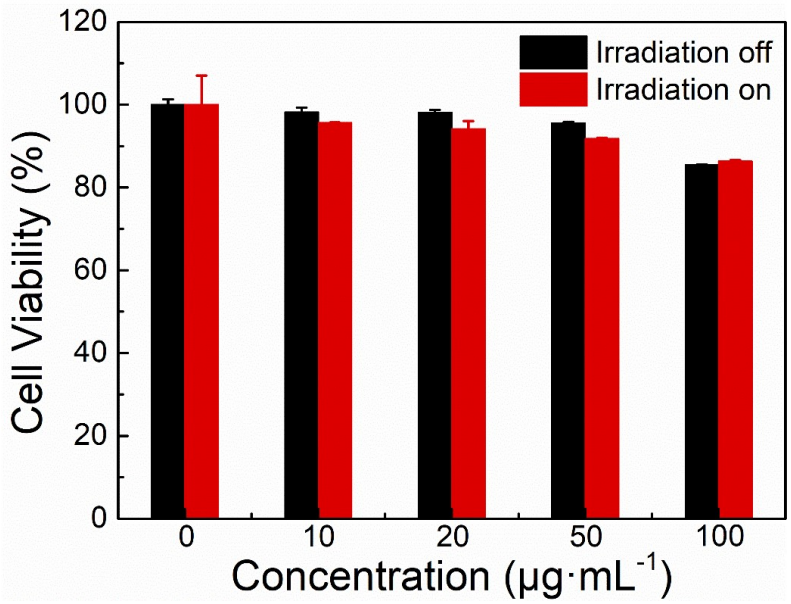

Figure S43. The viability of HeLa cells after incubation with DTPA-BT-F NCs for 24 h with or without light irradiation (400-800 nm; 100 mW·cm^{-2}, 5 min).

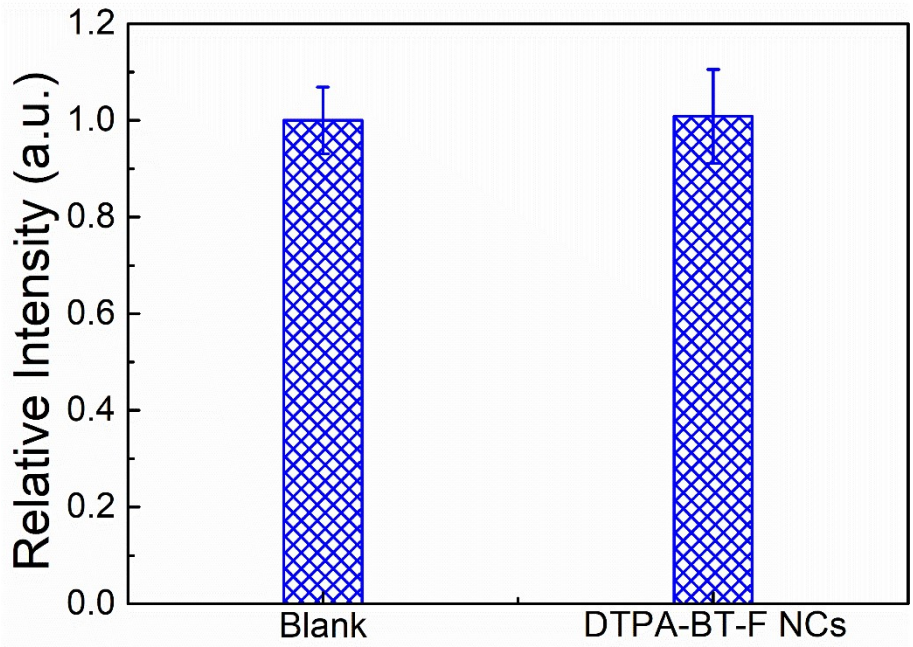

Figure S44. Relative fluorescence intensity of HeLa cells stained with LysoSensor Green DND-189 treated without (blank) and with DTPA-BT-F NCs.

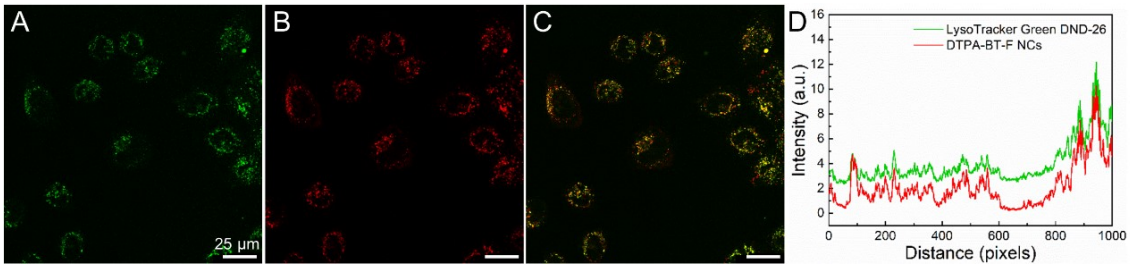

Figure S45. CLSM images of HeLa cells co-stained with LysoTracker Green DND-26 (A), DTPA-BT-F NCs (B), and their overlapped images (C); The intensity profile of the whole region in A and B recorded by ImageJ software (D).

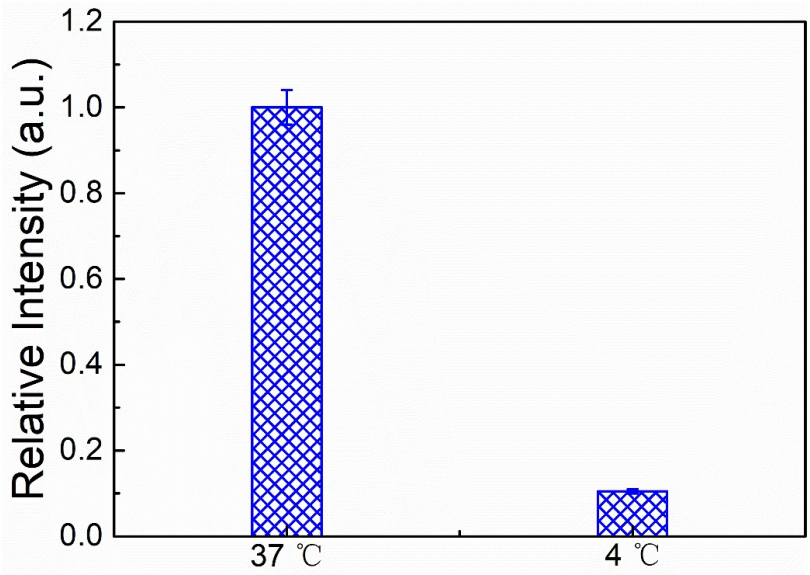

Figure S46. Relative fluorescence intensity of HeLa cells stained with DTPA-BT-F NCs incubated under 37 °C or 4 °C.

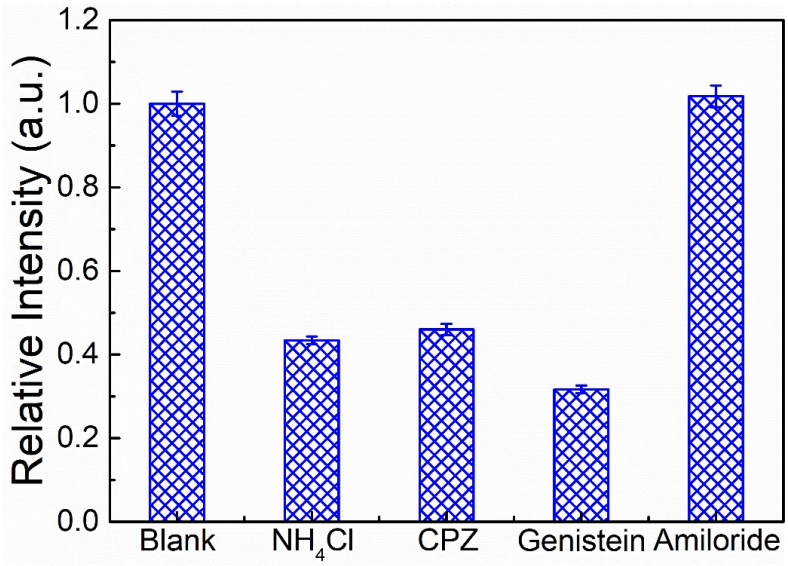

Figure S47. Relative fluorescence intensity of DTPA-BT-F NCs stained HeLa cells treated without (Blank) or with NH_4Cl (10 mM), CPZ (50 μM), genistein (150 μM) and amiloride (100 μM).

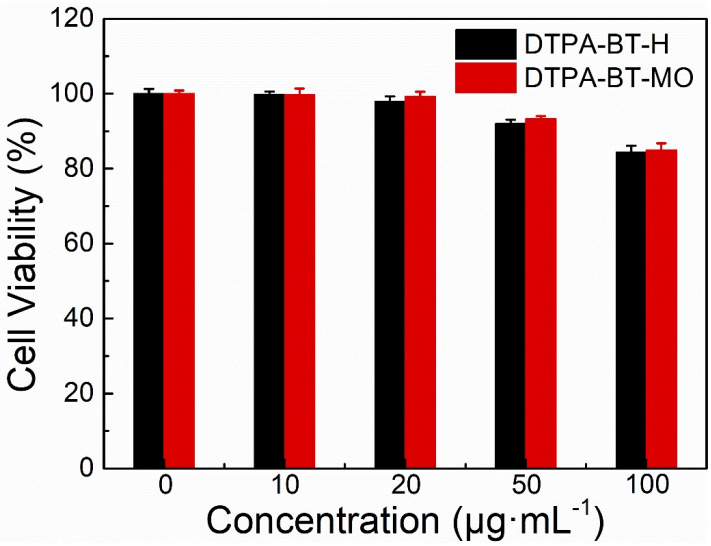

Figure S48. The viability of HeLa cells after incubation with DTPA-BT-H NPs and DTPA-BT-MO NPs for 24 h under different concentration.

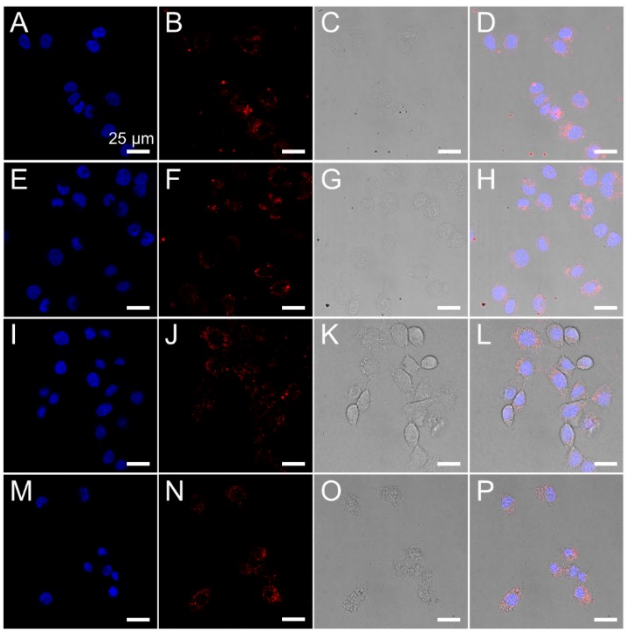

Figure S49. CLSM images of the fixed cells (A-H) stained with DAPI (blue) and DTPA-BT-H NPs (red, B and D) or DTPA-BT-MO NPs (red, F and H); CLSM images of the live cells (I-P) stained with Hoechst 33342 (blue) and DTPA-BT-H NPs (red, J and L) or DTPA-BT-MO NPs (red, N and P).

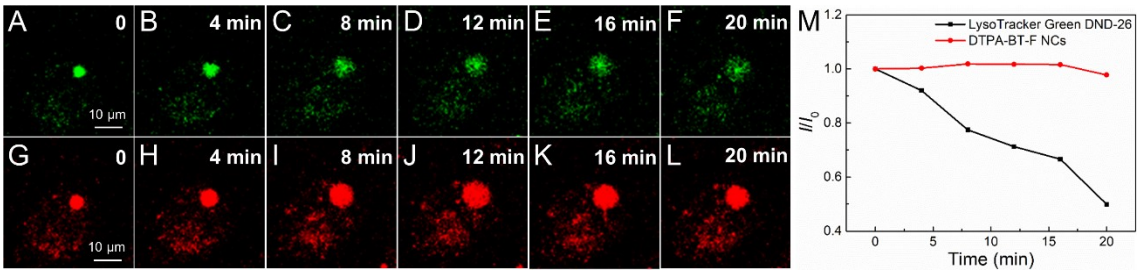

Figure S50. Time-dependent fluorescent images of HeLa cells co-stained with LysoTracker Green DND-26 (A-F) and DTPA-BT-F NCs (G-L) under the irradiation; Plots of I/I_0 values for LysoTracker Green DND-26 and DTPA-BT-F NCs stained cells under the irradiation (M).

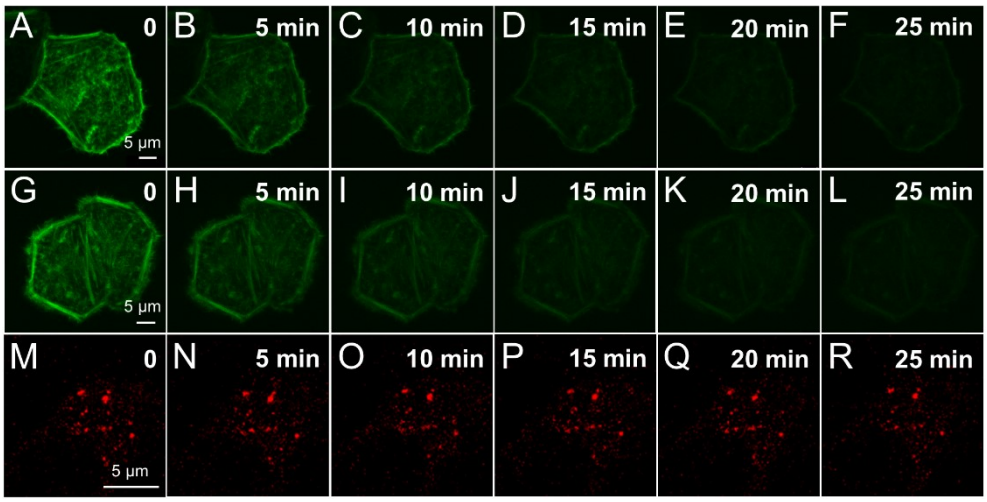

Figure S51. Time-dependent fluorescent images for FITC-Phalloidin (775 nm, 600 mW; A-F), Alexa Fluor488-Phalloidin (775 nm, 600 mW; G-L) and DTPA-BT-F NCs (775 nm, 600 mW; M-R) stained HeLa cells under the irradiation of STED beam.

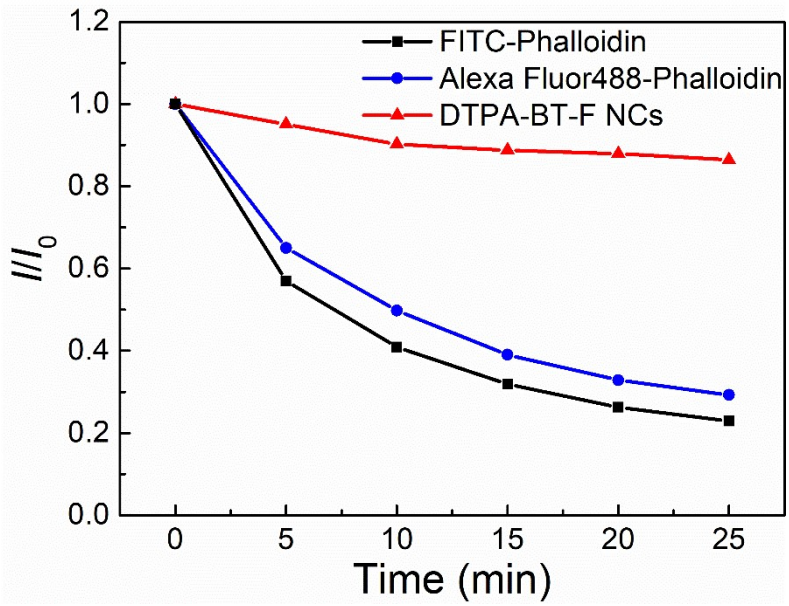

Figure S52. Plots of I/I_0 values for FITC-Phalloidin, Alexa Fluor488-Phalloidin and DTPA-BT-F NCs stained HeLa cells under the irradiation of STED beam (775 nm, 600 mW).

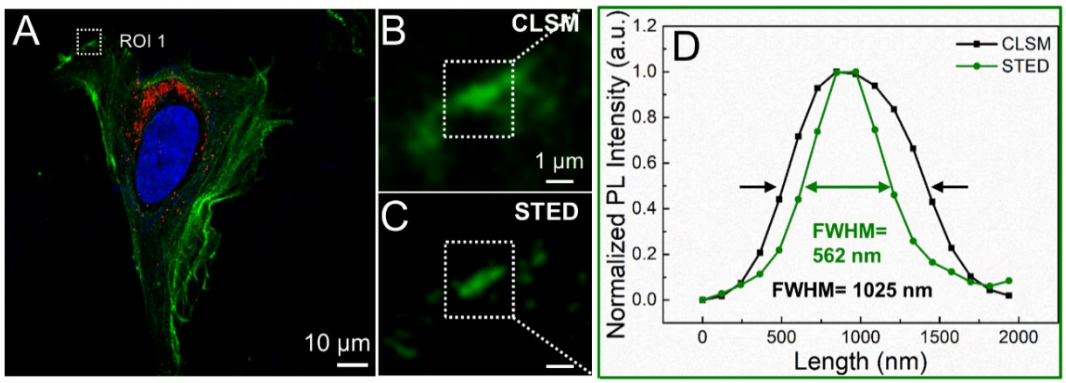

Figure S53. Fluorescence image of the fixed HeLa cell co-stained with DAPI (blue), FITC-Phalloidin (green; depleted by 592 nm STED laser, 120 mW) and DTPA-BT-F NCs (red; depleted by 775 nm STED laser, 96 mW) *via* STED nanoscopy (A); Magnified fluorescence images in FITC-Phalloidin channel by CLSM (B), STED nanoscopy (C), and their corresponding PL intensity curves (D) in A (ROI 1).

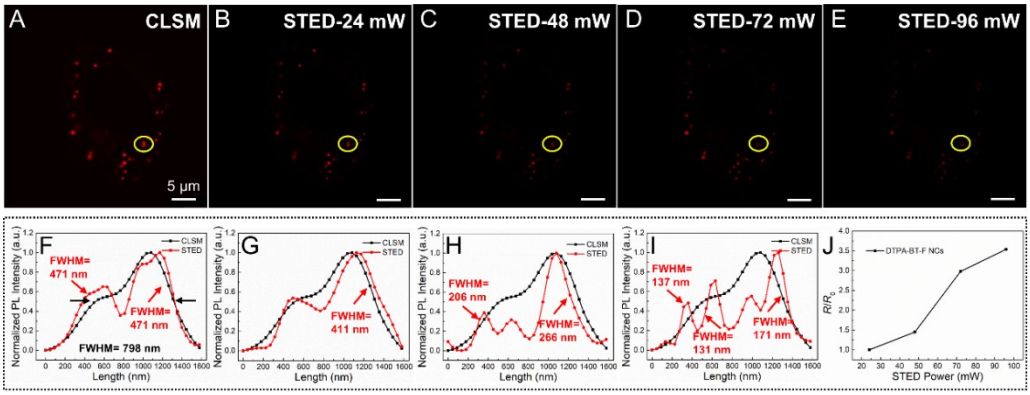

Figure S54. Fluorescence images of DTPA-BT-F NCs-stained cell captured by CLSM (A), STED nanoscopy under different beam powers (B-E), and their corresponding FWHM values in the ROI marked by yellow circle (F-I); Plot of lateral spatial resolution in B-E under STED nanoscopy versus STED power (J). The lateral spatial resolution is defined as R/R_0 value here, where R_0 is the FWHM difference between CLSM and STED mode at initial power (24 mW) and R is the FWHM difference at other powers (48, 72, and 96 mW).

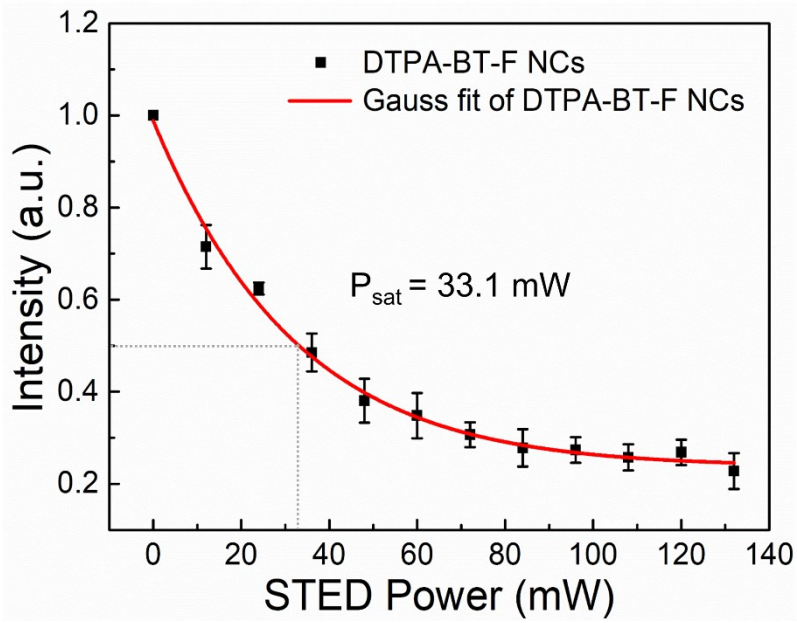

Figure S55. Power dependent depletion intensity for DTPA-BT-F NCs in STED nanoscopy.

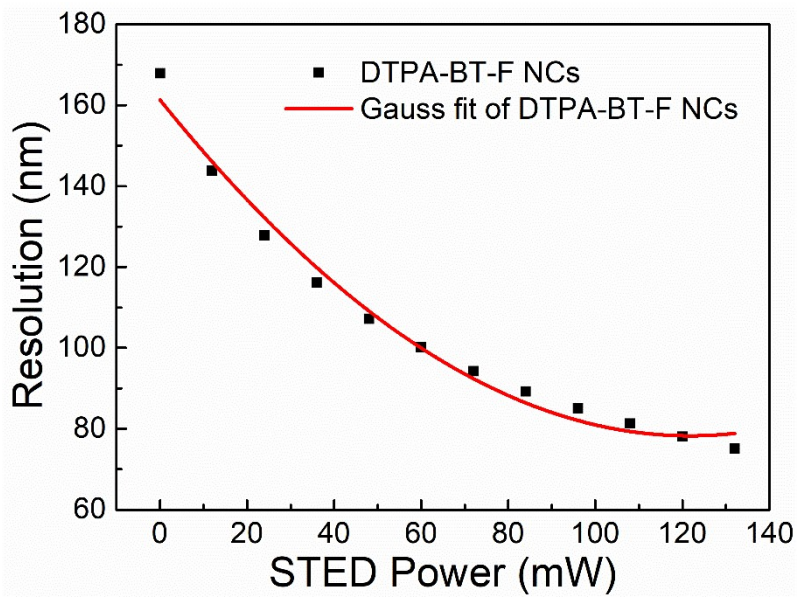

Figure S56. Theoretical resolution of DTPA-BT-F NCs under different STED power by the equation: $\Delta x \approx \frac{\lambda}{2NA\sqrt{1 + I / I_{sat}}}$.

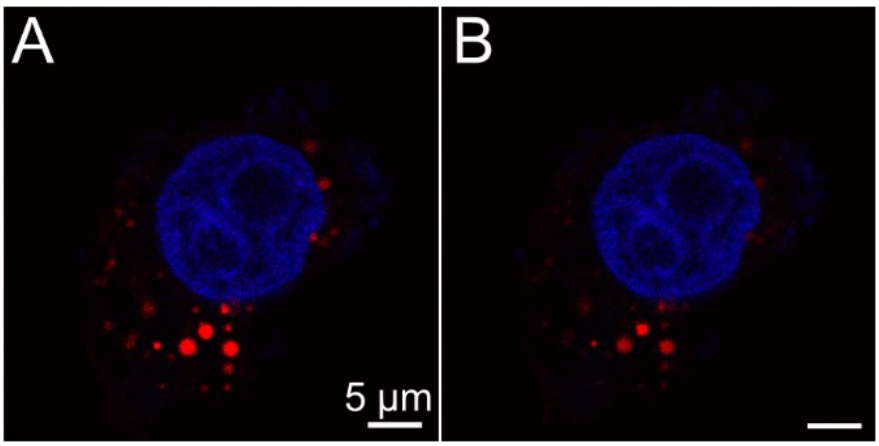

Figure S57. The live HeLa cells stained with Hoechst 33342 (blue) and DTPA-BT-F NCs (red) captured by CLSM (A) and STED nanoscopy (B) in 2D view.

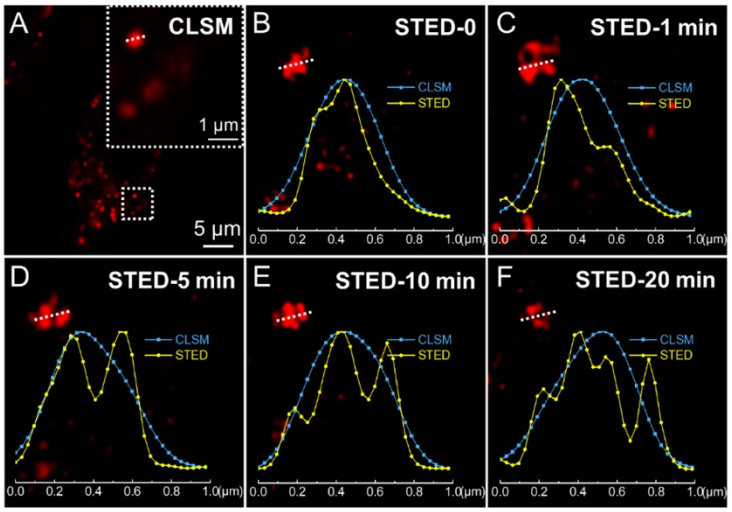

Figure S58. CLSM image of the live HeLa cell (A, the inset is the enlarged view of ROI marked by dashed square); Time-dependent STED images in ROI, and their corresponding intensity profiles along the dashed lines by CLSM and STED nanoscopy (B-F).

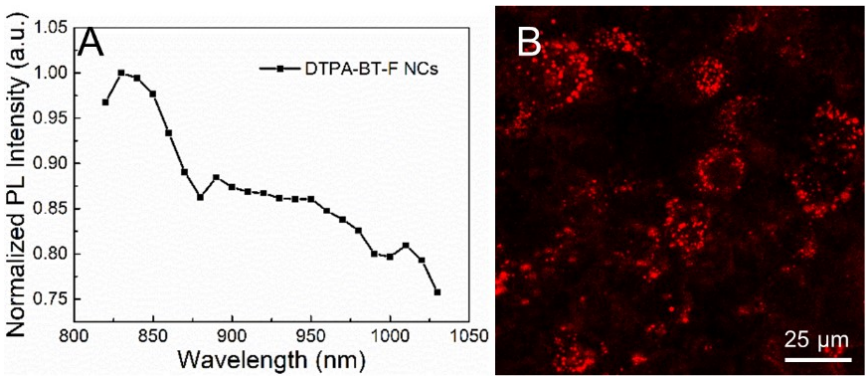

Figure S59. Normalized emission intensity of DTPA-BT-F NCs stained HeLa cells under different excitation wavelength (A); Fluorescent images of HeLa cells stained with DTPA-BT-F NCs (E_x: 830 nm; B) in TPF microscopy.

Table S1. Photo-physical properties of DTPA-BT-H, DTPA-BT-MO and DTPA-BT-F.

Samples	Stokes' shifts (nm/cm^{-1})	$\Phi^{[a]}/\Phi^{[b]}$ (%)	$\tau^{[a]}/\tau^{[b]}$ (ns)	$k_r^{[a]}$ ($\times 10^7$ s^{-1})	$k_r^{[b]}$ ($\times 10^7$ s^{-1})	$k_{nr}^{[a]}$ ($\times 10^7$ s^{-1})	$k_{nr}^{[b]}$ ($\times 10^7$ s^{-1})
DTPA-BT-H	196/6019	24.06/33.96	3.11/5.34	7.74	6.35	24.41	12.38
DTPA-BT-MO	204/6984	36.26/2.49	3.75/6.63	9.67	0.38	17.00	14.70
DTPA-BT-F	254/7597	4.03/36.49	1.03/4.22	3.91	8.65	93.17	15.04

[a] Measured in THF solution; [b] Measured in solids. Radiative decay rate: $k_r = \Phi/\tau$; Non-radiative decay rate: $k_{nr} = 1/\tau - k_r$.

Table S2. Photo-physical properties of DTPA-BT-H, DTPA-BT-MO and DTPA-BT-F in THF solution and in aggregated NPs or NCs state.

Samples	ε ($\times 10^3$ M$^{-1}\cdot$cm^{-1})	$\Phi^{[a]}$ (%)		L$^{[b]}$ ($\times 10^3$ M$^{-1}\cdot$cm^{-1})
	NPs or NCs	Solution	NPs or NCs	NPs or NCs
DTPA-BT-H	6.94	24.06	24.40	1.69
DTPA-BT-MO	6.39	36.26	14.18	0.91
DTPA-BT-F	13.10	4.03	27.06	3.54

[a] Photoluminescence quantum yield; [b] Fluorescence brightness (L), L= $\varepsilon \times \Phi$.